Development of hard and corrosion resistant titanium nitride thin films using high power impulse magnetron sputtering

by

Anas Ghailane

Accepted dissertation thesis for the partial fulfilment of the requirements for a

Doctor of Natural Sciences

Fachbereich 3: Mathematik/Naturwissenschaften

Universität Koblenz-Landau

Reviewers:

Dr. Christian B. Fischer

Prof. Dr. Jones Alami

Examiners:

Dr. Christian B. Fischer

Prof. Dr. Jones Alami

Prof. Dr. Wolfgang Imhof

Date of the oral examination: 15.03.2022

Declaration

I declare that this Ph.D. thesis entitled “Development of hard and corrosion resistant titanium nitride thin films using high power impulse magnetron sputtering” which I submit to Fachbereich 3: Mathematik / Naturwissenschaften of universität Koblenz-Landau for examination in consideration of the award of a higher degree (Doctor of Natural Sciences) is my own personal effort. The books and articles which I have made use of are acknowledged at the respective place in the text. For the present thesis, no degree or diploma or distinction has been conferred to me before, either in this or in any other university. I took reasonable care to ensure that the work is original, and, to the best of my knowledge, does not contravention copyright law, and has not been taken from other sources except where such work has been cited and acknowledged within the text.

Signature:

Student name: Anas Ghailane

Place and date: Koblenz, 21.03.2022

Schriftliche Darstellung zu dem eigenen Anteil:

Die zu verwendeten analytischen Methoden für diese Studie wurden durch den Autor der vorgelegten Thesis (Anas Ghailane) zusammen mit Prof. Dr. Jones Alami, Dr. Heinz Busch und Dr. Christian Fischer geplant.

Bei den Beschichtungen benutzte der Autor die dcMS und HiPIMS Prozesse am NTTF coatings GmbH in Rheinbreitbach und der UM6P in Benguerir, Marokko. Er führte die Charakterisierung der Beschichtungen durch und evaluierte die erhaltenen Messdaten. Die Messungen der Härte, zum Korrosionsverhalten und der Schichtdicke wurden durch den Autor durchgeführt und ausgewertet. Die hier gezeigten REM-Messungen erfolgten sowohl selbständig als auch mit Unterstützung von Herrn Dr. Heinz Busch. Die XRD Messungen sowie Raman Spektroskopie wurden von Dr. Youssef Tamraoui und Dr. Said Mansouri durchgeführt, die Auswertung der Daten führte den Autor.

Die hier vorgelegte Dissertation wurde vollständig durch den Autor verfasst und konzipiert.

Koblenz, der 21.03.2022 Anas Ghailane

Abstract in English

To render the surface of a material capable of withstanding mechanical and electrochemical loads, and to perform well in service, the deposition of a thin film or coating is a solution. In this project, such a thin film deposition is carried out. The coating material chosen is titanium nitride (TiN) which is a ceramic material known to possess a high hardness (>10 GPa) as well as good corrosion resistance. The method of deposition selected is high power impulse magnetron sputtering (HiPIMS) that results in coatings with high quality and enhanced properties. Sputtering is a physical process that represents the removal or dislodgment of surface atoms by energetic particle bombardment. The term magnetron indicates that a magnetic field is utilized to increase the efficiency of the sputtering process. In HiPIMS, a high power is applied in pulses of low duty cycles to a cathode that is sputtered and that consists of the coating material. As result of the high power, the ionization of the sputtered material takes place giving the possibility to control these species with electric and magnetic field allowing thereby the improvement and tuning of coating properties. However, the drawback of HiPIMS is a low deposition rate.

In this project, it is demonstrated first that it is possible to deposit TiN coating using HiPIMS with an optimized deposition rate, by varying the magnetic field strength. It was found that low magnetic field strength (here 22mT) results in a deposition rate similar to that of conventional magnetron sputtering in which the average power is applied continuously, called also direct current magnetron sputtering (dcMS). The high deposition rate at low magnetic field strength was attributed to a reduction in the back attraction probability of the sputtered species. The magnetic field strength did not show noticeable influence on the mechanical properties. The proposed explanation was that the considered peak current density interval 1.22-1.72 $A \cdot cm^{-2}$ does not exhibit dramatic changes in the plasma dynamics.

In a second part, using the optimized deposition rate, the optimized chemical composition of TiN was determined. It was shown that the chemical composition of TiN does not significantly influence the corrosion performance but impacts considerably the mechanical properties. It was also shown that the corrosion resistance of the coatings deposited using HiPIMS was higher than that of the coatings deposited using dcMS.

The third study was the effect of annealing post deposition on the properties of TiN coating deposited using HiPIMS. The hardness of the coatings showed a maximum at 400°C reaching 24.8 GPa. Above 400°C however, a lowering of the hardness was measured and was due to the oxidation of TiN which led to the formation of TiN-TiO_2 composites with lower mechanical properties.

The coating microscopic properties such as crystal orientation, residual stresses, average grain size were determined from X-ray diffraction data and the roughness was measured using atomic force microscopy.

These properties were found to vary with the magnetic field strength, the chemical composition as well as the annealing temperature.

Abstract auf Deutsch

Um die Oberfläche eines Werkstoffes so zu gestalten, dass sie mechanischen und elektrochemischen Belastungen standhält und im Betrieb optimal funktioniert, bietet sich die Abscheidung einer dünnen Schicht oder eines Überzugs an. In der vorliegenden Arbeit wird eine entsprechende Dünnschichtabscheidung durchgeführt. Als Beschichtungsmaterial wird Titannitrid (TiN) gewählt, ein keramisches Material, von dem bekannt ist, dass es eine hohe Härte (> 10 GPa) sowie eine gute Korrosionsbeständigkeit besitzt. Das gewählte Abscheidungsverfahren ist das Hochleistungs-Impuls-Magnetron-Sputtern (HiPIMS), welches zu Beschichtungen mit hoher Qualität und verbesserten Eigenschaften führt. Das Sputtern ist ein physikalischer Prozess, der das Entfernen oder Umlagern von Oberflächenatomen durch den Beschuss mit energetischen Teilchen darstellt. Der Begriff Magnetron weißt darauf hin, dass ein Magnetfeld eingesetzt wird, um die Effizienz des Sputterprozesses zu erhöhen. Bei HiPIMS wird eine hohe Leistung in Pulsen von kurzer Dauer an die zu sputternde Kathode angelegt, die aus dem Beschichtungsmaterial besteht. Aufgrund der hohen Leistung findet eine Ionisierung des besputterten Materials statt, was wiederum die Möglichkeit eröffnet die entstandenen Spezies mit einem elektrischen und magnetischen Feld zu kontrollieren und dadurch die Beschichtungseigenschaften zu verbessern und abzustimmen. Der Nachteil des HiPIMS-Prozesses ist jedoch eine geringe Abscheiderate.

In diesem Projekt wird erstmals gezeigt, dass es möglich ist, TiN-Beschichtungen mittels HiPIMS mit einer optimierten Abscheiderate, durch Variation der Magnetfeldstärke, abzuscheiden. Es zeigte sich, dass eine geringe Magnetfeldstärke (hier 22mT) zu einer Abscheiderate führt, die der des konventionellen Magnetron-Sputterns ähnlich ist, bei dem die mittlere Leistung kontinuierlich angelegt wird, auch Gleichstrom-Magnetron-Sputtern (dcMS) genannt. Die hohe Abscheiderate bei niedriger magnetischer Feldstärke wurde einer Verringerung der Rückanziehungswahrscheinlichkeit der gesputterten Spezies zugeschrieben. Die magnetische Feldstärke zeigte keinen merklichen Einfluss auf die mechanischen Eigenschaften. Die vorgeschlagene Erklärung war, dass das betrachtete Spitzenstromdichteintervall 1.22-1.72 $A \cdot cm^{-2}$ keine dramatischen Änderungen in der Plasmadynamik zeigt.

In einem zweiten Teil wurde mit der optimierten Abscheiderate die optimierte chemische Zusammensetzung von TiN bestimmt. Es zeigte sich, dass die chemische Zusammensetzung von TiN das Korrosionsverhalten nicht wesentlich beeinflusst, jedoch die mechanischen Eigenschaften erheblich verändert. Es zeigte sich auch, dass die Korrosionsbeständigkeit, der mit HiPIMS abgeschiedenen Schichten höher war als die der mit dcMS abgeschiedenen Schichten.

Die dritte Studie war die Wirkung des Glühens nach der Abscheidung auf die Eigenschaften der mit HiPIMS abgeschiedenen TiN-Beschichtung. Die Härte der Beschichtungen zeigte ein Maximum bei 400°C und erreichte 24.8 GPa. Oberhalb von 400°C wurde jedoch eine Verringerung der Härte gemessen, die auf die

Oxidation von TiN zurückzuführen war, die zur Bildung von TiN-TiO_2-Kompositen mit geringeren mechanischen Eigenschaften führte.

Die beschichtungsmikroskopischen Eigenschaften wie Kristallorientierung, Eigenspannungen, durchschnittliche Korngröße wurden aus Röntgenbeugungsdaten bestimmt und die Oberflächenrauheit wurde mittels Rasterkraftmikroskopie gemessen. Es wurde festgestellt, dass diese Eigenschaften mit der magnetischen Feldstärke, der chemischen Zusammensetzung sowie der Glühtemperatur variieren.

The results obtained in the present work were published in peer reviewed journals according to the following list:

- **Anas Ghailane**, Olayinka Abegunde, Hicham Larhlimi, Chaymae Hejjaj, Mohammed Makha, Heinz Busch, Christian B. Fischer, Jones Alami, Titanium nitride,$Ti_xN_{(1-x)}$, coatings deposited by HiPIMS for corrosion resistance and wear protection properties, Appl. Surf. Sci. 574 (2022) 151635. https://doi.org/10.1016/j.apsusc.2021.151635 (IF 2022 6.707).

- **Anas Ghailane**, Maadane El Yazid, Ayyoube Barchid, Sabah Berchane, Soukayna Badre-Eddine, Hicham Larhlimi, Christian B. Fischer, Mohammed Makha, Jones Alami, Influence of annealing temperature on the microstructure and hardness of TiN coatings deposited by HiPIMS, J. Mater. Eng. Perform. (2021). https://doi.org/10.1007/s11665-022-06689-5 (IF 2022 1.819).

- **Anas Ghailane**, Mohammed Makha, Hicham Larhlimi, Jones Alami, Design of hard coatings deposited by HiPIMS and dcMS, Mater. Lett. 280 (2020) 128540. https://doi.org/10.1016/j.matlet.2020.128540 (IF 2022 3.423).

- **Anas Ghailane**, Hicham Larhlimi, Youssef Tamraoui, Mohammed Makha, Heinz Busch, Christian B. Fischer, Jones Alami, The effect of magnetic field configuration on structural and mechanical properties of TiN coatings deposited by HiPIMS and dcMS, Surf. Coat. Technol. 404 (2020) 126572. https://doi.org/10.1016/j.surfcoat.2020.126572 (IF 2020 4.16).

The publications in which I have participated:

- Hicham Larhlimi, **Anas Ghailane**, Mohammed Makha, Jones Alami, Magnetron sputtered titanium carbide-based coatings : A review of science and technology, Vacuum. 197 (2022) 110853. https://doi.org/10.1016/j.vacuum.2021.110853 (IF 2022 3.627)

- Mohammed Makha, **Anas Ghailane**, Hicham Larhlimi, Jones Alami, Emerging opportunities for 2D-black phosphorus as a carrier transporting material in perovskite solar cells, Mater. Lett. 276 (2020) 128234. https://doi.org/10.1016/j.matlet.2020.128234 (IF 2022 3.423)

- Mohammed Makha, **Anas Ghailane**, Hicham Larhlimi, Heinz Busch, Jones Alami, Phosphorus Containing Coatings: Technologies and Applications, Chem. Select. 5 (2020). https://doi.org/10.1002/slct.202001214 (IF 2020 2.0).

Acknowledgment

I gratefully acknowledge the help of my supervisor Prof. Dr. Jones Alami during this project. He was always a technical and a personal advisor to me. The discussions were always providing more ideas, deeper reflections, as well as clarifications to scientific concepts. I thank him for his time and consideration, which was constantly present through the entire period of the project.

I thank Dr. Heinz Busch for welcoming me to his company to work with the coating equipment and for the many insightful discussions.

I should thank Dr. Christian Fischer for supervision and for examination of this thesis.

Thanks goes also to Dr. Olayinka Abegunde, Prof. Mohammed Makha, M.Sc. Hicham Larhlimi and all my colleagues at the department of materials science, energy and nanoengineering of Mohammed VI Polytechnic University (UM6P).

I would like to also to thank my brother Amine Ghailane for his help whether financial or moral, and I thank all my family for their support.

I would like to thank UM6P for financing this thesis.

I dedicate this thesis to the memory of my father.

Contents

Introduction 1
1. Process of thin film deposition 2
1.1. Magnetron sputtering 2
1.2. Reactive magnetron sputtering 10
1.3. Thin film microstructure 13
1.4. High Power Impulse Magnetron Sputtering 15
1.4.1. Self-sputtering in HiPIMS 18
2. Experimental 19
2.1. Sample preparation 19
2.2. Deposition set-up and process parameters 20
2.2.1. Deposition series at NTTF coatings, GmbH, Germany 20
2.2.2. Deposition series at UM6P, Morocco 23
3. Thin film characterization 26
3.1. Mechanical properties (Nano-indentation) 26
3.2. Corrosion resistance 28
3.3. Structural analysis 33
3.3.1. X-ray diffraction (XRD) 33
3.3.2. Scanning electron microscopy 38
3.3.3. Atomic force microscopy 40
3.3.4. Raman spectroscopy 42
4. Summary of the results 44
5. Conclusion 50
6. References: 52
7. Scope of the papers 59
8. Appendix 61

Introduction

Surface treatment concerns the use of mechanical, chemical, electrochemical, or physical techniques to modify the properties of a surface of a material, in order to meet the requirements of a given application. Deposition of thin films is a surface treatment approach that consists of applying a thin layer of a specified material to cover a substrate, in order to give it improved surface properties such as corrosion resistance, wear resistance, or other mechanical, optical or electrical properties. Thin films usually have thicknesses ranging between a few nm to a few µm. There are several technologies used to deposit thin films including chemical vapor deposition (CVD) and physical vapor deposition (PVD) [1]. In both techniques a vapor of the material to be deposited is created and then transported onto a substrate in the form of individual atoms or molecules [1]. The main difference resides in the way by which the vapor is created. In CVD the vapor is obtained by chemical means, through the reaction of a suitable gas precursor with a suitable gas reactant, depending on the coating [2][3]. In PVD, the vapor is typically created by physical means through heat (thermal evaporation) [4] or by energetic particle bombardment (sputtering) [5]. Both CVD and PVD are used to deposit customized coatings for demanding applications, due to the high level of control of the deposition process that could be achieved. However, the CVD process requires high temperatures to activate the chemical reaction in the gas phase. For example, the process temperature range for TiN is from 850°C to 1100°C which makes the CVD technique not suitable for temperature sensitive substrates, for example [6]. In the case of PVD, the TiN coating can be deposited at relatively low substrate temperatures ranging between 350°C and 450°C [6]. Typically, PVD TiN is deposited using cathodic arc evaporation (CAE) or direct current magnetron sputtering (dcMS), and exhibits generally excellent mechanical properties [7]. Coatings deposited by CAE exhibit typically a dense and nano-grained structure while in dcMS the coatings are of lower density and show typically a columnar structure [8]. The latter contains micro voids and low-density areas between columns. Both methods are successfully implemented in industry and find more and more uses, as incremental technical innovations are being adopted.

Both CAE and magnetron sputtering are being tested for diffusion barrier coatings application. However, due to the deposition of defects such as macro-droplets emanating from the cathode during CAE [9], these coatings are yet to show their suitability for anti-corrosion applications. Conventional magnetron sputtering typically results in coatings with columnar structures with low-density inter-columnar areas that constitute diffusion channels for the corrosive agents when exposed to a corrosive environment. To address some of the shortcomings of conventional magnetron sputtering, scientists at Linköping University in Sweden introduced a new deposition technique, namely high-power pulsed

magnetron sputtering (HPPMS) also known as HiPIMS [10]. HiPIMS is characterized by high electron density in the plasma (typically of 10^{13} cm^{-3}), compared to dcMS where the electron densities typically ranges around $10^{10}cm^{-3}$[10]. As a result of the high electron density, the electron impact ionization probability is promoted in HiPIMS and leads to a high ion fraction of the sputtered species (up to 90% for Ti) compared to dcMS (less than 1%) [10]. During HiPIMS, the power is applied to the target in short pulses of some µs, at a low duty cycle below 10% and with a frequency lower than 2 kHz [10]. This guarantees a very high peak power density in the range of a few $kW{\cdot}cm^{-2}$ without overheating the target and exceeding the Curie temperature of the magnetron's magnets. The large ion fraction gives a better control of the energy bombardment of the growing film, and subsequently its properties [10]. The high-flux ion bombardment of a growing film results in substantial momentum transfer to the adatoms of the growing surface which increases their mobility, leads to a high film density, and allows the engineering of the growing film's grain size and grain boundary as well as the resulting stress profile [11][12][13], which in turns provides tools to design tailor-made mechanical characteristics [11][12][13]. As far as corrosion resistance is concerned, a thin film with high density should provide a better performance as the diffusion of the corrosive agent through the pores is hindered, which increases the performance of the coating in a corrosive environment [14].

The thesis work addresses the issue of corrosion resistance and wear resistance of thin films prepared using HiPIMS. First a literature review was done to highlight the advantages of HiPIMS over dcMS regarding the thin film properties. This is the subject matter of paper I. Prior to characterizing the corrosion properties, it is demonstrated through paper II, that an improvement of HiPIMS deposition rate is possible through the variation of the magnetic field strength of the magnetron's magnetic setup. The material chosen was TiN as it is a wear resistant ceramic coating as highlighted in paper I. In paper III the corrosion and mechanical properties of TiN deposited at different nitrogen flow rates are studied to examine the effect of the nitrogen content on these properties. Finally, a study of the effect of annealing temperature on the mechanical properties of TiN coatings using HiPIMS is made (Paper IV).

1. Process of thin film deposition

1.1. Magnetron sputtering

The first reported sputter deposition was performed in 1934 by Hulburt in a residual atmosphere of air where opaque, optically good films were deposited by sputtering of various metals such as antimony, bismuth, cadmium, gold, lead, platinum, silver, tin, zinc, and carbon. Sputtering in air for

over 30 hours from graphite yielded nearly opaque carbon films. The author suggested that probably the sputtered films were mostly carbon, although they may possibly have contained some hydrocarbons formed by the combination of carbon with the residual gases in the sputtering chamber [15]. To deposit coatings with better purity, sputtering under vacuum is necessary [16]. Due to improvement in vacuum technology in the late 1950s and early 1960s [17], DC sputtering was used to deposit conductive materials [17], and radio frequency sputtering was utilized to deposit insulating materials [18].

The working principle of the sputtering deposition process is as follows: 1. A deposition chamber is evacuated to a high vacuum using vacuum pumps; 2. An inert gas, typically argon, is introduced into the chamber [19], using a mass flow controller [16]; 3. A negative voltage typically of 2000 - 5000 V is applied to a cathode consisting of the material to be deposited [19]; 4. The positive terminal of the DC power supply is connected to ground [19] usually via the chamber walls; 5. The substrate can be grounded, biased, or electrically insulated [20]; 6. Finally, an electric field is created between the cathode and the substrate. As a result, the electrons flow from the cathode to the anode and during their course, they interact with argon atoms ejecting an electron from the outer shell of these atoms creating thereby argon ions. The mixture of ions, electrons, neutrals and other species is referred to as plasma [21]. The sputtering process starts when ions in the vicinity of the target surface are accelerated towards the target surface by and electric field that forms between the plasma and the target. The ionic bombardment causes ejection of target atoms, that are transported through the plasma and deposit on all surfaces, including the substrate [22].

Figure 1 shows schematically how the sputtering of surface atoms occurs (through collision cascade) by bombardment with an energetic ion [22]. The number of sputtered atoms ejected per one ion incident is called the sputtering yield and is a function of the incoming ion energy and its mass, the mass of the surface atom and the binding energy of the target atoms [23].

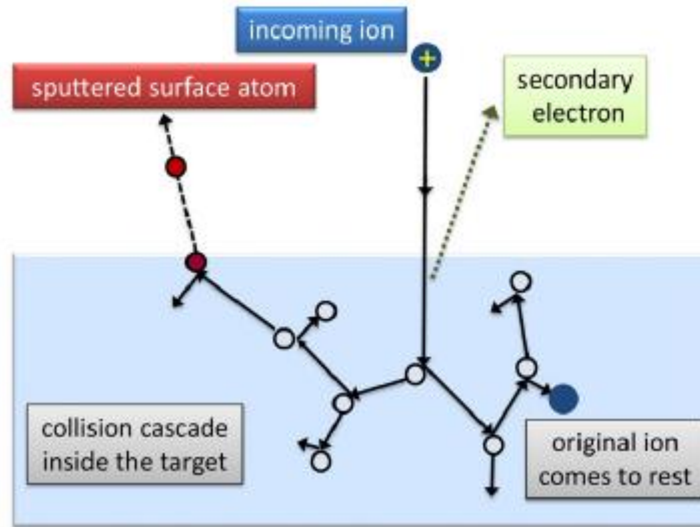

Figure 1: Schematic illustration of the interaction between an energetic bombarding particle and the surface of a target illustrating the sputtering process [22].

There is a minimum threshold energy that the incident ion should have in order to cause sputtering of the target atoms. This energy is related to the surface binding energy of the target atoms and depends on the mass of both the projectile and target atoms [22] [23].

The sputtering yield is a function of the threshold energy, the energy of the incident ion, the mass of the incoming ion, the target atoms, and the surface binding energy [23]. This is expressed in the following formula:

$$Y = (6.4 \,.\, 10^{-3}) m_r \gamma^{\frac{5}{3}} E^{0.25} (1 - \frac{E_{th}}{E})^{3.5} \qquad \text{Equation 1}$$

Where Y the sputtering yield, E the initial energy of the incident atom in electron volts, m_r the projectile mass in atomic mass unit, and γ is the energy mass transfer defined as:

$$\gamma = \frac{4 m_r m_p}{(m_r + m_p)^2}$$

E_{th} is the threshold energy for sputtering defined by Bohdansky's expression [23]:

$E_{th} = \frac{U_{sb}}{\gamma(1-\gamma)}$ for $\frac{m_p}{m_r} < 0.3$ and $E_{th} = 8U_{sb} (\frac{m_p}{m_r})^{2/5}$ for $\frac{m_p}{m_r} > 0.3$

where U_{sb} the surface binding energy of the target atoms and is effectively the heat of sublimation per particle.

A sputtering yield calculator C++ program based on equation 1 is given in the appendix.

In addition to sputtering, secondary electron emission also takes place when the incoming ion hits the surface of the target as seen in figure 1. The emission of secondary electrons are very important as they participate in the ionization process, producing more free electrons and ions and thus sustaining the plasma discharge [22].

As seen in Figure 2, there are different spaces in the chamber that appear between the cathode and anode. We distinguish between the space containing the plasma and plasma sheaths in the vicinity of the target, substrate, and chamber walls. To understand the reasons why sheaths are formed, first note that the electron thermal velocity is at least 100 times the ion thermal velocity because of the mass difference [21]. Because the net charge density in the plasma is zero (quasi neutral), the electric potential and the electric field is zero everywhere. Hence, the fast-moving electrons are not confined and are lost near the walls. As a result, thin positively charged layers (sheaths) form near each wall [21] because the ions are attracted by the electrons and so the density of ions is higher than the density of electrons within the sheath. The electric field within the sheaths point from the plasma to the wall [21], which gives the plasma a potential voltage that is higher than the potential of the chamber walls and the substrate [20]. Therefore, when the chamber is grounded, the plasma potential will be positive.

An ion that is outside the plasma sheath is not going to be attracted by the electric field at the target and thus will not participate in the process of sputtering. The sheath thickness depends on the discharge current density, the voltage drop across the cathode and the ion mass [24].

If the substrate is electrically insulated (floating) in the chamber, it will be charged by the fast-moving electrons, attract ions, and repel electrons until the flux of electrons and ions become equal i.e., no net current is flowing. The substrate is said to be at a floating potential [20] .

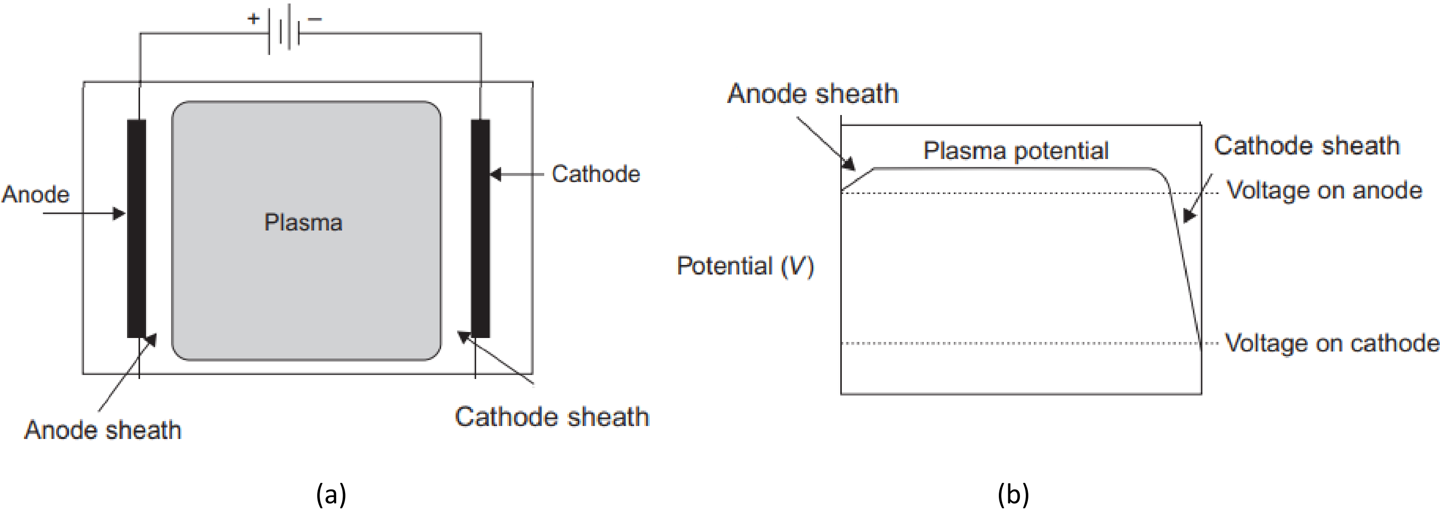

(a) (b)

Figure 2: Schematic illustration of (a) simplest type of sputtering apparatus consisting of two plates, a vacuum chamber, and a power supply. A sputtering gas, typically argon, is introduced and voltage is applied across the plates. (b) plot of the potential distribution along the centerline of the apparatus. Adapted from [25].

The energetic secondary electrons during a sputtering deposition are not used efficiently for ionization and are lost to the walls and the substrate instead of participating in the ionization [19][24]. As a result, a sufficiently high working gas pressure is required in order to increase the ionization probability [19]. The sputtering process usually operates at a pressure window between 2 and 4 Pa [19] [26]. However, at this pressure the cathode sheath is collisional as its thickness is about 1-2 cm whereas the ion neutral mean free path is below 1 cm [19][24]. Due to this collisional sheath in which the collision occurs between the accelerating ions and working gas neutrals, the ions bombard the target surface with a broad energy spectrum [19]. As a result, the energy of the sputtered species will be low. This energy, at high pressure, is also lowered by subsequent scattering of the sputtered species with the working gas [19]. This has a consequence on the growing film as the sputtered species do not have enough momentum to transfer to the adatoms essential for the diffusion of the adatoms on the film surface to grow dense films as will be seen in section 1.3.

Another consequence of this high deposition pressure (2-4Pa), is the low deposition rate [19]. As a consequence of the difficult ionization due to high scattering of the working gas atoms between themselves and with the sputtered atoms, a low secondary electron flux is available which necessitates a high discharge voltage in order to overcome the electrical breakdown voltage of the working gas [19].

In order to overcome some of the drawbacks of the sputtering process, including the low deposition rate, the high discharge voltage and the high required deposition pressure, scientists developed magnetron sputtering. The latter makes use of permanent magnets, placed behind the deposition target, to confine negatively charged electrons in the vicinity of the sputtering target. Magnetron sputtering was developed during the 1960s and 1970s [19]. As the name indicates, the magnetron involves magnets placed behind the target and consists of an inner and outer magnet arranged with opposite polarity as shown in Figure 3 [24]. This configuration of the permanent magnets results in the confinement of electrons in the immediate vicinity of the target through the Lorentz force [27] , as per equation 2:

$$F = q(E + v \; x \; B) \qquad \text{Equation 2}$$

where F the Lorentz force, E the electric field, q the charge of the particle, v the velocity of the charged particle and B the magnetic field flux density.

The magnetic field component that is perpendicular to the electric field gives the electrons a direction that is perpendicular to both the electric field and the magnetic fields. This keeps the electrons orbiting the target in a motion known as gyration characterized by a gyration radius that is given in Equation 3, where $r_{g,e}$ the gyration radius, m_e is the mass of an electron, and e the elementary charge [22]. Electrons are thus confined in the target vicinity. The velocity of the resulting ExB drift is given by Equation 4 [22].

$$r_{g,e} = \frac{m_e v}{eB} \qquad \text{Equation 3}$$

$$v_{ExB} = \frac{ExB}{B^2} \qquad \text{Equation 4}$$

The magnetic induced confinement of the electrons increases their residence time, which allows multiple collision events with the working gas and increases the gas and sputtered atoms ionization probability [22].

As a result of the increased ionization rate, the current increases, the voltage needed to start the plasma decreases, and the pressure needed to start the plasma is reduced [19].

Planar dcMS sources are commonly operated in the pressure range 0.2–4 Pa with a cathode voltage in the range of 300–700 V. The resulting discharge current densities are in the range 4–60 mA.cm^{-2} and power densities of several tens of W.cm^{-2} [19] [24]. For the lowest working gas pressure (0.2Pa), the mean free path for the sputtered atoms is 10 – 15 cm while at the highest pressure (4Pa), the mean free path is below 1 cm [19]. Thus for depositions using the lowest working gas pressure (0.2Pa), the deposition of the thin film is a line-of-sight process whereas in the case of higher pressure (4Pa) the sputtered atoms undergo collision with the working gas and are therefore considered ‘thermalized’ [28], loosing thereby their directionality. In magnetron sputtering, the electron density can reach values of between 10^{15} m^{-3} and 10^{17} m^{-3}. However, at this electron density, the ionization degree of the sputtered species is very low (< 2%), and the substrate’s bombarding species are mainly the noble working gas [19].

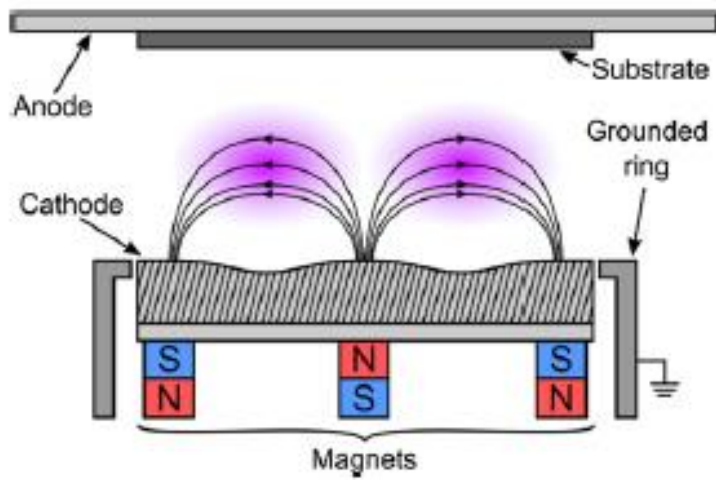

Figure 3: Schematic representation of cross-sectional view of the planar magnetron sputtering.

There are different types of magnetrons, classified according to the magnetic strength and the degree of unbalance. In the balanced configuration, the strength of the outer magnet is equal to the strength of the inner magnets. In the unbalanced magnetron, the strength of the outer magnet is higher than that of the inner magnet and the field lines coming from the outer magnet are not coupled to the inner magnet but enter the opposite pole of the outer ring magnets. This magnetron is called unbalanced type II [27]. Another type of the unbalanced configuration (not often used) has a stronger inner magnet and is called unbalanced type I. Figure 4 shows the different types of magnetrons (balanced, unbalanced type I and unbalanced type II).

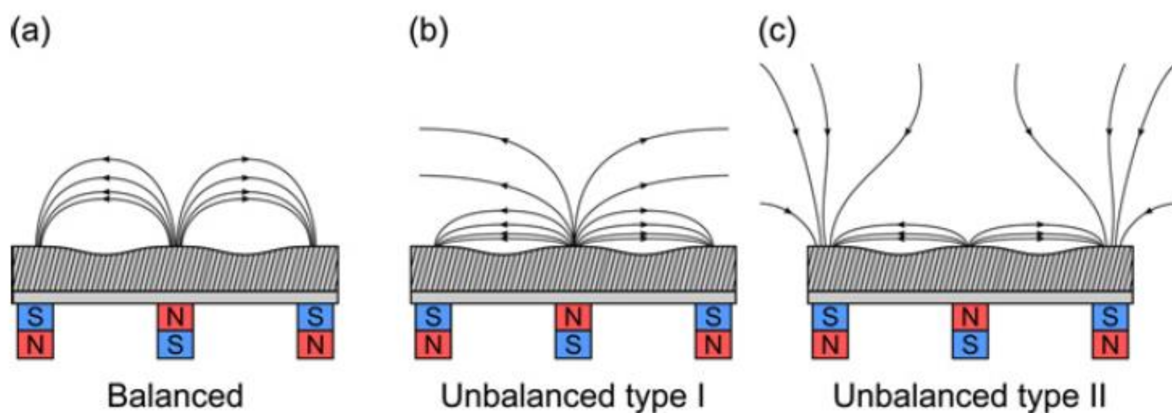

Figure 4: Schematic representation of the three types of the planar magnetron sputtering discharge [24].

The magnetic field configuration plays an important role in the plasma dynamics; the more the magnetron is unbalanced (type II), the more focused the ionized species are towards the substrate, and the more efficient the momentum transfer to the adatoms at the growing surface [29].

Alami et al. [27] did FEM simulation of four possible magnetic field configurations. The simulations are shown in Figure 5. As we can see the strength of the magnetic field at the target was set by increasing the distance of the magnet from the target. For the unbalanced case, the inner magnet is at a distance from the target, higher than the distance of the outer magnet from the target. Figure 5 shows that the configuration with the highest number of field lines closed in the center is the strongly balanced (S-B) configuration.

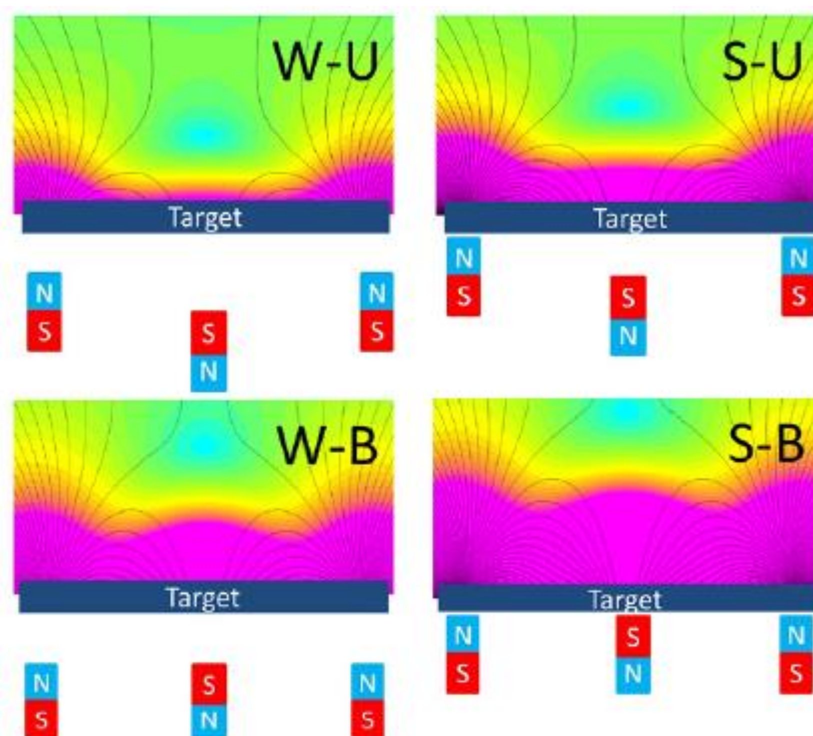

Figure 5: Magnetic field simulations (obtained by finite element method magnetics software) of four possible magnetic field configurations (weak/ strongly unbalanced W–U, strong/strongly unbalanced S–U, weak/slightly unbalanced W–B, strong/slightly unbalanced S–B, according magnet arrangement) [27].

The magnetic field unbalancing degree for the unbalanced magnetron type II (see Figure 4) can be characterized by two parameters which are the imbalance coefficient K and the geometrical imbalance coefficient K_G [6] [27] [30].

The imbalance coefficient is defined as the ratio between the magnetic flux of the outer magnet and the magnetic flux of the inner magnet:

$$K = \frac{H_2}{H_1} = \frac{\int B_2 dS_2}{\int B_1 dS_1} \quad \text{Equation 5}$$

Where B_1 the magnetic flux density flowing perpendicular to the surface S_1 of the inner magnet and B_2 the magnetic flux density flowing perpendicular to the surface S_2 of the outer magnet. H_1 and H_2 are magnetic field intensities of the outer and the inner magnets, respectively.

The coefficient of geometrical imbalance is defined as:

$$K_G = \frac{Z_0}{2\bar{R}} \quad \text{Equation 6}$$

With Z_0 being the distance between the magnetic field zero and the surface of the target. And $\bar{R}$ is the radius of the erosion rill on the target.

Figure 6 [30] illustrates the distance, Z_0, the surfaces S_1 and S_2 as well as B_1 and B_2.

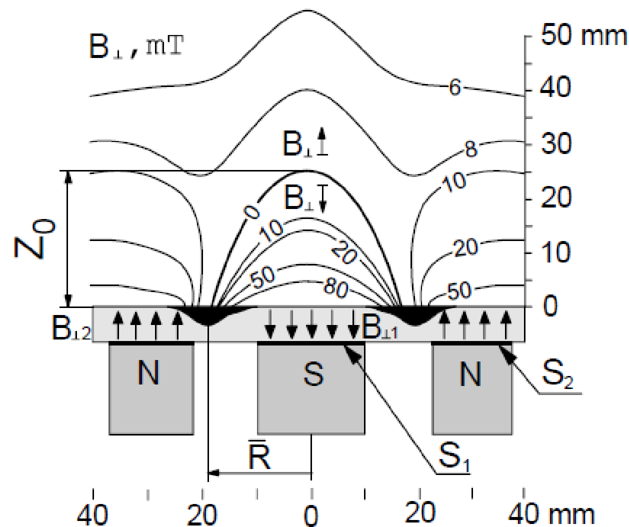

Figure 6: Distribution of the magnetic field flux density perpendicular to the permanent magnets [30].

1.2. Reactive magnetron sputtering

The deposition of chemical compound thin film is a necessity in many applications, especially when mechanical as well corrosion properties are required. Most of the important thin films are chemical compounds [31]. To deposit chemical compound thin film, reactive magnetron sputtering is preferred

because the compound can be prepared from a low-cost metal target instead of an expensive ceramic one, by the admission of a suitable reactive gas into the chamber in addition to the working gas. Oxides such TiO_2 and nitrides such as TiN, CrN are the most common materials deposited by reactive sputtering [32]. Other chemical compounds such as carbides [33] and sulphides [34] are also deposited. In this part, the characteristics of a reactive magnetron sputtering are explained.

The reaction between the reactive gas and the sputtered species does not occur in the gas phase as the energy and momentum cannot be conserved in a two-body collision [35]. Therefore, a third body is needed for the chemical reaction to occur. Surfaces can act as a third body for the reaction [19]. So, when the reactive gas is admitted into the chamber, the reaction with the sputtered metal atom at the substrate surface takes place but also reaction with the chamber walls and the target surface occurs.

Due to the reaction at the target surface, the sputtering yield and the yield of secondary electrons are altered as they depend on the material and therefore the discharge parameters are affected. One refers to "poisoning of the target" when a compound layer is formed on the target surface [22]. Figure 7 [24] illustrates the change of the yield of secondary electrons emission (SEE) of the compound with respect to that of different metals. As it can be seen, in the case of titanium the SEE yield for compound forming (here oxide or nitride) is lower than that of the metal.

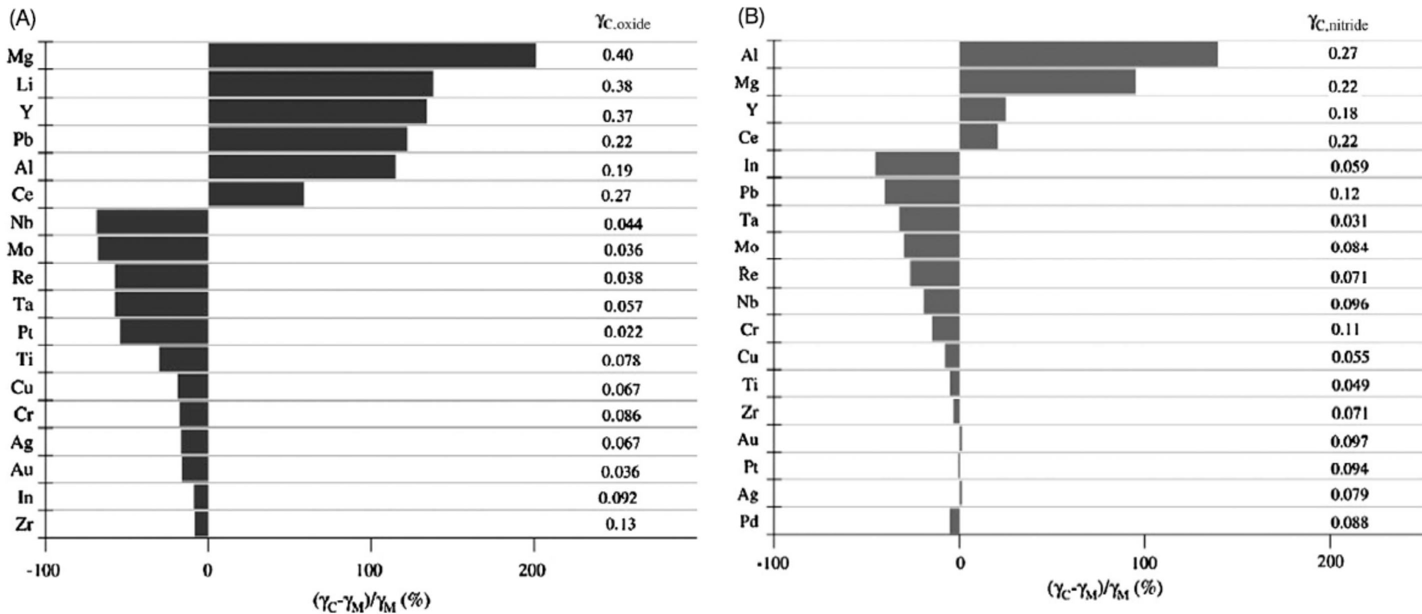

Figure 7: Change of SEE yield when depositing (A) oxides and (B) nitrides [24].

Concerning the sputtering yield of the compound material, it is usually considerably lower than the sputtering yield of the elemental target material. Furthermore, low SEE yield lowers the ionization rate and thus the sputtering rate. Consequently, the deposition rate decreases as the amount of reactive gas increases in the chamber. Furthermore, less atoms of the elemental target material are sputtered and thus less reactive gas material is consumed which results in a sharp increase of the reactive gas partial pressure [19]. Figure 8 shows the change in deposition process parameters upon the supply of reactive gas oxygen for the deposition of TiO_2 [24].

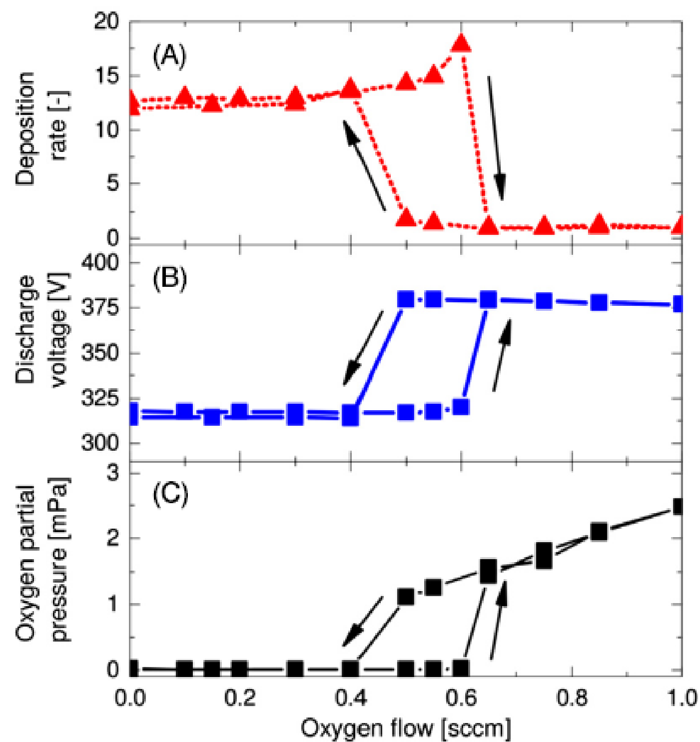

Figure 8: Evolution of process parameters (A) deposition rate, (B) discharge voltage, and (C) oxygen partial pressure with the oxygen flow rate in reactive sputtering of Ti in Ar/O_2 atmosphere. The arrows indicate the direction of the transition [24].

As it can be seen from Figure 8, the operating parameters namely the deposition rate (Fig. 8A), the discharge voltage (Fig. 8B) and the reactive gas partial pressure (Fig. 8C) exhibit a nonlinear response as a function of the reactive gas flow rate. This nonlinear response is referred as hysteresis curve [22]. The operation of a reactive magnetron sputtering process can be divided into three main parts. For low reactive gas flow, ions arriving at the target surface sputter away the few surface atoms that have reacted with the reactive gas. As a result, the surface of the target remains metallic and due to the high yield of metal sputtering and electron emission, as explained above, the deposition rate is high

[24]. The process is referred as metallic mode sputtering characterized by a high deposition rate (Fig. 8A) [24]. In this mode, the reactive gas may react at the substrate surface but the resulting film will be under stoichiometric [24]. Concerning the discharge voltage (Fig. 8B), the values are low in the metallic mode, most likely because of the high current provided by the high SEE yield of the metal that the target is consisted of [24]. Due to low reactive gas oxygen flow rate, the process is still starved from oxygen and as a result the oxygen partial pressure is low (Fig. 8C) [24].

As the reactive gas flow rate is enhanced, the deposition rate increases slightly since the mass of the reactive gas atoms adds to that of the deposited metal [19]. Further increase in the reactive gas flow rate results in an abrupt decrease in the deposition rate. This is due to the fact that a compound forms on the target as the sputtering of surface atoms that have reacted with oxygen cannot keep up with the formation of compound material on the target, and a transition from metal to compound mode occurs [22]. The discharge voltage increases abruptly as well, and this can be attributed to the decrease in current as the SEE yield is reduced upon compound formation on the target surface [24]. Since the target is now poisoned i.e. contaminated with compound, the flux of metal atom coming from the target is strongly reduced which result in a diminution of the uptake of reactive gas by the sputtered metal [22]. This leads to an abrupt increase of the reactive gas partial pressure (Fig. 8C) until pumping of the gas and flow of the gas balance [24].

Decreasing the flow rate will bring the system back into the metallic mode. However, the reversal to metallic mode does not occur before the compound mode has been removed from the target. Therefore, a hysteresis occurs, illustrating the dependence of the operating discharge parameters on the direction of change [22].

The hysteresis effect is simply due to a competition between two opposing processes: the formation of a compound on the target surface and the sputtering of the compound from the target surface [22].

1.3. Thin film microstructure

One of the determining criteria of thin film quality is its density, which gives to the thin film enhanced mechanical as well as improved diffusion barrier properties essential for corrosion resistance purposes. The surface mobility of the adatoms is the driving force for dense thin films. Surface mobility is achieved and increased by supplying energy to the adatoms. Thornton classified the thin film microstructure, representative of the thin film density, according to the supply of energy to the adatoms in two forms: heat supplied by increase in temperature and energy attained through decrease

in momentum loss by the reduction of pressure. Figure 9 illustrates the structural zone model as elaborated by Thornton [36] [37].

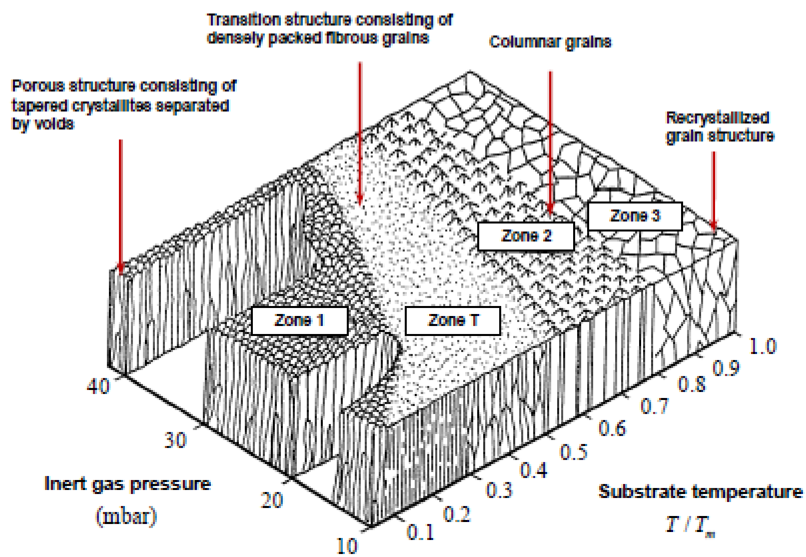

Figure 9: Structural zone model [37].

There are four different zones (1, T, 2, 3) in the structural zone model (Fig. 9). Zone 1 is a porous structure consisting of tapered crystallites separated by voids. This zone is promoted as the temperature is reduced and as the pressure is increased. This is because at high pressure – low substrate temperature, the energy of the adatoms is very low to cause sufficient surface diffusion to fill up the voids.

Zone T consists of densely packed fibrous grains. The adatom mobility is still limited, but here the voids are narrower.

In zone 2 and 3 the increasing substrate temperature leads to increasing surface diffusion of the growing film. Zone 2 starts at $T_S/T_M > 0.3$ (with T_S the substrate temperature and T_M the melting temperature of the film). Atoms migrate to grains that are energetically favorable resulting in large columnar grains. The grain boundaries are thinner than in the case of zones 1 and T. The grain size increases with increasing T_S/T_M. Zone 3 starts at $T_S/T_M > 0.5$ in which grains are less columnar and the structure is recrystallized to new crystals. A polycrystalline structure similar to the bulk polycrystalline structure is obtained.

To calculate the thermal velocity provided to the adatom upon supply of temperature, one can use Equation 7 derived from kinetic gas theory [38].

$$v_{th} = \sqrt{\frac{2k_B T}{m}} \qquad \text{Equation 7}$$

In which: k_b the Boltzman Constant $= \frac{R}{N_a} = 1.38\text{x}10^{-23}$, where R is the universal gas constant and N_a, the Avogadro number.

To obtain zone 3 the condition $T_S/T_M > 0.5$ should be fulfilled. For example, at $T_S/T_M=0.7$ in the case of Titanium, $T_S = 1941$ K, the velocity calculated using Equation 7 is:

$$\boldsymbol{v_{th}} = \sqrt{\frac{2 * (1.38x10^{-23}) \left[\frac{J}{K}\right] x\ 1941[K]}{47{,}8\ x\ 1{,}67x10^{-27}[kg]}} = 819\ m.s^{-1}$$

However, 1941 K is a high temperature for temperature sensitive substrates. As a result, the electrical energy can be provided efficiently instead, to supply the same kinetic energy and provide the same thermal velocity. In fact, a small electrical energy of 0.17 V can provide a velocity of 819m/s to the adatoms instead of using a temperature of 1941 K. This is demonstrated using Equation 8.

$$\frac{1}{2} m \boldsymbol{v_{th}}^2 = k_B T = qxU \qquad \text{Equation 8}$$

For $v_{th} = 819 m.s^{-1}, U = \ 0.17\ V$

For the electrical energy to be operative on the atoms, they need to be charged. Therefore, it is of high interest to ionize the atoms of the thin film source. This provides them with electrical energy that will increase their kinetic energy and as result their mobility on the surface of the growing film, thus improving the compactness of the film.

1.4. High Power Impulse Magnetron Sputtering

As seen in section 1.3, ionizing the sputtered species allows the sputtered species themselves to be mobile during growth as the electrical energy will be effective on these ionized species. Furthermore, the ionized flux of sputtered species allows efficient momentum transfer to the adatom as their mass is equal to the mass of the projectile [39]. In a conventional dcMS process, it is possible to increase the flux of ions to the substrate by increasing for example the unbalancing degree of the magnetron. However, most of the ionized flux to the substrate is made of Ar^+ ions which can result in undesired

implantation of Ar^+ ions and degradation of the film structure especially if a bias voltage is applied [39]. Therefore, HiPIMS is used to allow the flux of ions to the substrate to be made mostly from sputtered species. This is more desirable to enhance the film microstructure to zone 3 (Figure 9) as explained in section 1.3, improving thereby the coating properties without the need to supply heat [40]. In fact, the electron density in HiPIMS can reach 10^{13} cm^{-3} [10] and atoms in such dense plasma can have a high ionization probability through electron impact [22] [39].

In order to avoid target overheating (melting) and exceeding the Curie temperature T_C of the magnetron's magnets that lead to their demagnetization, the high power in HiPIMS is applied in pulses of low duty cycle in the range of 0.5 to 5% [24], to allow the target to cool down during the pulse off-time. The average power is maintained similar to that of dcMS while the peak power density can be in the range of 0.1 $kW.cm^{-2}$ [41] to 10 $kW.cm^{-2}$ [24]. The pulse on-time of the HiPIMS discharge ranges typically from few tens up to several hundreds of microseconds, with repetition frequencies of tens of Hz to several kHz [20].

The HiPIMS process was first established by Kouznetsov et al. at Linköping university [42]. The invented approach of HiPIMS necessitates a DC power supply connected to a pulsing unit [24]. The DC power supply loads a capacitor bank that deliver energy to transistors that act as switch with a switching capability in the microsecond range. This approach was named high power impulse magnetron sputtering (HiPIMS). It allows the ionization of the sputtered species by increasing the power to high level, which leads to an increase in the electron density and thus the ionization probability. This is achieved without overheating the target as the high power is applied only in pulses with low duty cycle.

The schematic representation of the HiPIMS set-up is shown in Figure 10 [24]. The pulse generation set-up utilizes a large capacitor C that is loaded from a regular DC power supply V_Z. The capacitor is connected to the magnetron by a transistor switch S via an inductor L. The waveforms of discharge voltage and current for present circuit are shown in Figure 11 [24]. During the pulse, a large discharge current I_D, can be generated by the capacitor when charged to the voltage V_C. The pulse current I_D is many times higher than the maximum DC current supplied by the DC source since a large energy can be stored in the capacitor C. The energy stored in the capacitor is given by Equation 9.

$$\varepsilon_c = \frac{1}{2} C {V_c}^2 \qquad \text{Equation 9}$$

Adding an inductor L between the switch S and the cathode (Fig. 10) allows controlling (slowing down) the rate of current increase in the discharge and helps partially protect the transistor switch from large current surges [24]. The voltage V_i induced by the inductor which is oriented against the current change depends on the discharge current I_D and the inductance L (see Equation 10).

$$I = -\frac{dI_D}{dt}L \quad \text{Equation 10}$$

The inductance L is also used to partially avoid undesirable arc characterized by a very high discharge current and a low discharge voltage [24]. The typical current and voltage waveforms can be found in Figure 11. This configuration exhibits a rather rectangular voltage pulse V_D and a slow growth of the discharge current I_D during the pulse. The growth rate of I_D during the pulse is determined by the size of the inductor L and the plasma impedance of the magnetron sputtering discharge.

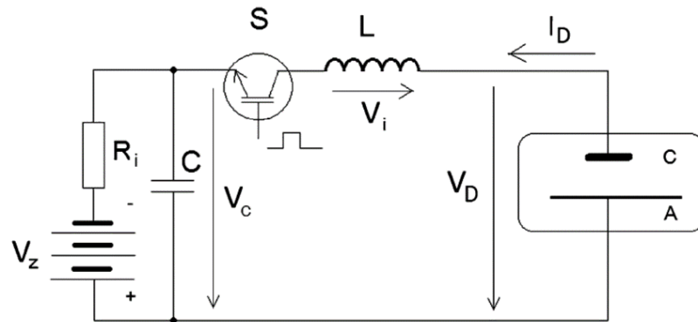

Figure 10: Schematic representation of a HiPIMS set-up [24].

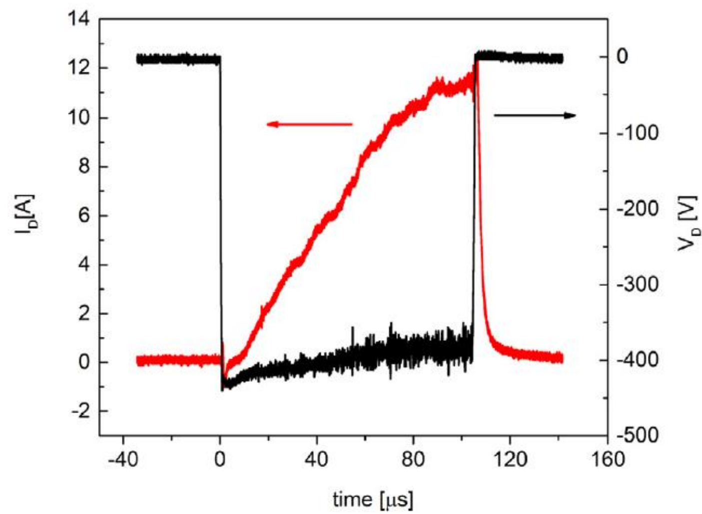

Figure 11: The discharge voltage and current waveforms measured on the magnetron cathode from a pulsed power supply as depicted in Fig. 10 [24].

1.4.1. Self-sputtering in HiPIMS

As the target species are ionized in HiPIMS, they can be accelerated by the negatively biased target and participate to sputtering of the target which is called self-sputtering [22]. This paradigm is a drawback in HiPIMS as it reduces the deposition rate since the metal species are back attracted to the target instead of reaching the substrate to grow as a coating.

The magnetic field strength and the magnetron's unbalancing degree are very important parameters in the control of self-sputtering [6]. The magnetic field influences the fraction of the ions that stays in the target area, and what fraction escapes to the substrate to benefit from ion flux assistance to the growing film [22]. Generally, a stronger magnetic field leads to higher ionization but also to a greater back-attraction of ions to the target: one obtains higher self-sputtering and lower deposition rate. The unbalancing degree should also be high enough to allow more ionization in the substrate vicinity [22].

Figure 12 graphically illustrates a target material model for HiPIMS that was developed by Christie [43] and further improved by Vlcek et al. [44]. This model illustrates which fractions of particles has to be maximized and which has to be minimized in order to increase the deposition rate in HiPIMS.

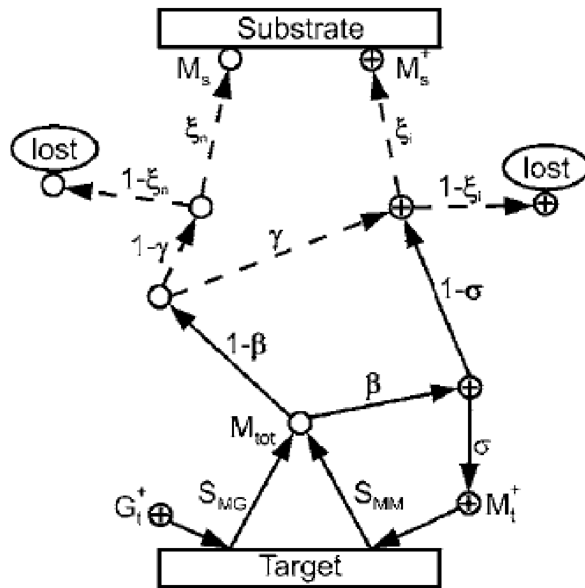

Figure 12: Schematic illustration of the phenomenological model used for HiPIMS [44]. Modifications of the original model, developed by Christie [42], are denoted by dashed lines.

Referring to Figure 12, the variables used in the model are described: ${G_t}^+$ is the number of process gas ions hitting the target. S_{MG} is the sputtering yield of the target material by process gas ions defined

such that S_{MG}> 0. S_{MM} is the sputtering yield of the target material for sputtering by target metal ions (self-sputtering yield), defined such that S_{MM}> 0. ${M_t}^+$is the number of target material ions hitting the target. M_{tot} is the total number of target material atoms sputtered from the target by the combination of process gas ions and target material ions. There is a probability β that the target atoms M_{tot} becomes ionized. With a probability $(1-\beta)$ the atoms remain neutral. The term σ is the probability that an ionized metal is back attracted to the target to participate in sputtering i.e. to become ${M_t}^+$ In other words, it is the fraction of βM_{tot} that is redirected to the target upon ionization. Then, with a probability of ($1-\sigma$) the metal ions will go to the substrate. This is then the fraction of βM_{tot} that is directed to the substrate. The fraction $(1-\beta)\ M_{tot}$ that was not ionized near the target can get ionized in the vapor phase on the way to the substrate by a probability of ionization γ. The probability that $(1-\beta)\ M_{tot}$ will get lost instead of getting ionized is then $(1-\gamma)$.
The fraction $\gamma(1-\beta)\ M_{tot}$ can get lost with a probability of $(1-\xi_i)$ and a fraction ξ_i will reach the substrate. The fraction $(1-\gamma)(1-\beta)\ M_{tot}$ will reach the substrate by a probability of ξ_n and a fraction $(1-\xi_n)(1-\gamma)(1-\beta)\ M_{tot}$ will get lost.
The decrease in the magnetic field strength increases the deposition rate because the product of ionization probability β by back-attraction probability σ is reduced, and therefore number of particles $\beta\sigma M_{tot}$ are reduced [6] [45].

2. Experimental

2.1. Sample preparation

Prior to deposition, the surface of the samples was prepared by grinding and polishing followed by a cleaning in isopropanol for 10 min in ultrasonic bath. The next step was cleaning using etching. Etching is defined as material removal from a surface via energetic particle bombardment [46].

At UM6P, an etching procedure is established which consists of the following steps (compare Fig. 13):

- Connect the negative terminal of the pulsing unit to one target and the positive terminal to the opposite target
- Send a bipolar HiPIMS pulse to the pulser to allow electrons to oscillate between both targets with shutters closed to avoid deposition.
- Apply a current to coils placed as shown in Figure 13 that create magnetic field lines perpendicular to the normal of the targets. The magnetic field traps electrons near the substrate and create ionization at this vicinity producing argon ions for etching.

- Apply a negative substrate bias.

- The pressure, the power at the target, and the current at the coils were optimized with respect to the etching rate and were chosen to be 3 kW, 1.5.10^{-3} mbar, 75 A and yielded an etching rate of 100 nm.h^{-1}.

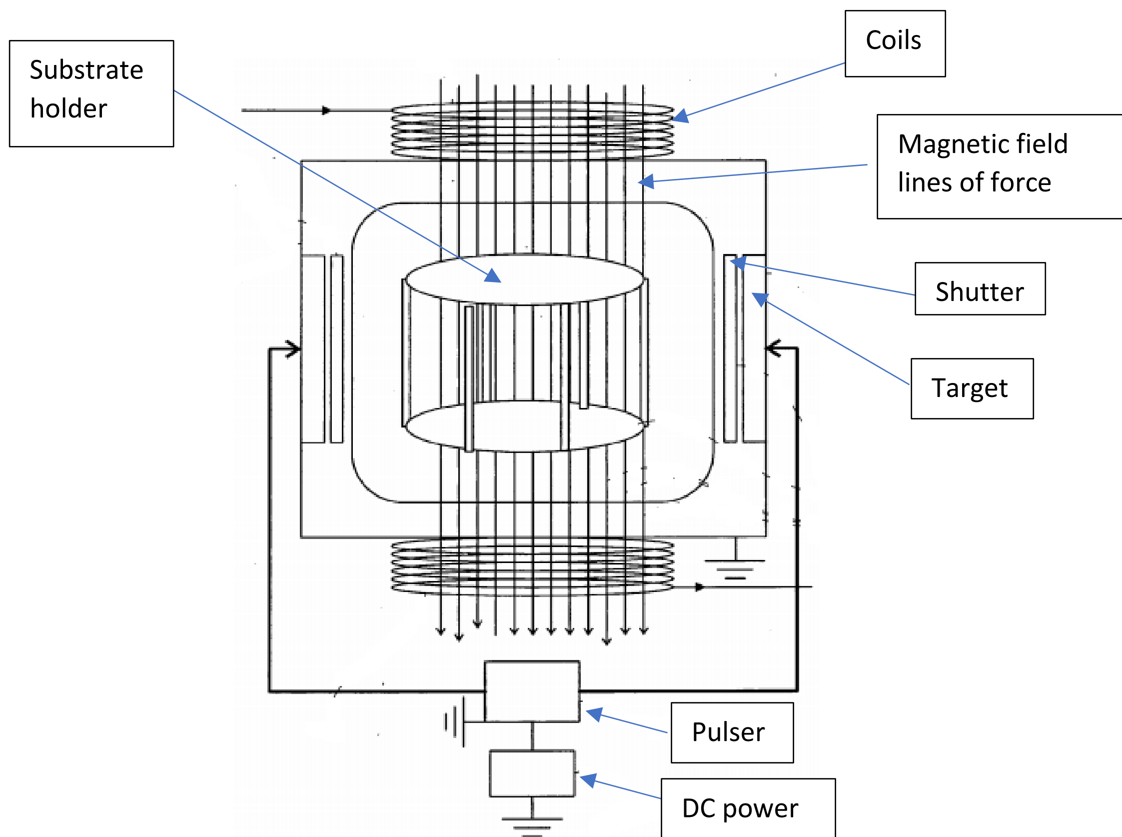

Figure 13: Schematic of the cross section of a sputtering chamber illustrating the etching components (Adapted from reference [47]).

2.2. Deposition set-up and process parameters

2.2.1. Deposition series at NTTF coatings GmbH, Germany

The results obtained in reference [6] were achieved using the HiPIMS deposition configuration shown in Figure 14 situated at NTTF coatings GmbH, Germany. The HiPIMS set-up consisted of a DC power supply (GX-ADL GmbH, Germany) connected to the target via a pulsing unit (SPIK1000A-MELEC GmbH, Germany). The pulsed signal functions were generated by an arbitrary waveform generator unit (AFG 2005-GW INSTEK Ltd.; USA). For dcMS depositions, the power was supplied by a PFG 5000 power supply (Hüttinger Elektronik GmbH, Germany). The size of the vacuum chamber is 45 x 45 x 45 cm^3.

Prior to deposition the substrates were etched with argon plasma using a radio frequency plasma source placed in the chamber as shown in Figure 14. The pumping is done using a rotatory vane pump (up to 1 Pa) supported by a turbo molecular pump (up to 10^{-3} Pa). The working gas and the reactive gas were supplied to the chamber in metered quantities using mass flow controllers (TPG 261 A, Pfeiffer, Germany).

The target and the substrate were placed parallel to each other, and the target-to-substrate distance was set at 9 cm. The average power was kept constant at a value of 600 W for all depositions. The substrate holder was kept stationary without rotation during deposition.

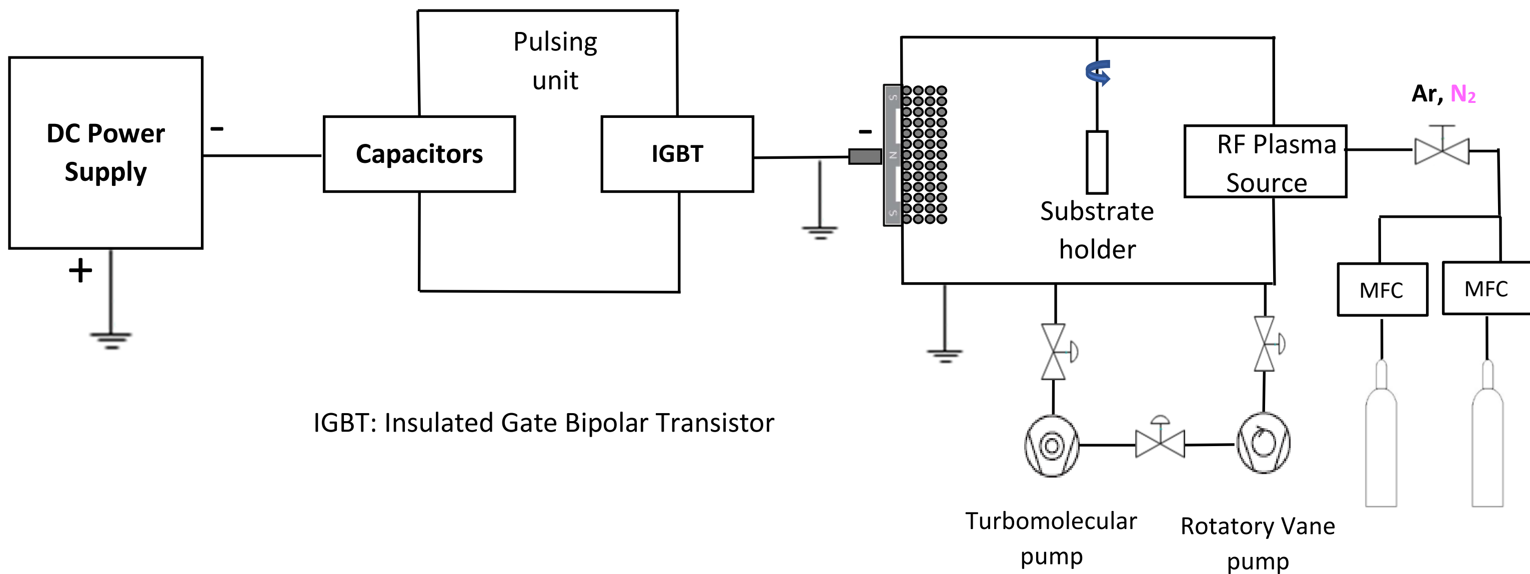

Figure 14: Deposition set-up for the study of the effect of magnetic field strength ([6]).

The parameter that was studied in reference [6] using the set-up of Figure 14 was the magnetic field strength Φ. Table 1 shows the current and voltage values as a function of Φ for the HiPIMS case and Table 2 for the dcMS case. In both HiPIMS and dcMS the average power was maintained constant at 600 W, the pressure was around $1.8.10^{-1}$ Pa, and the target-to-substrate distance was maintained at 9 cm. The peak current and power densities were calculated with respect to the racetrack area which is 60.3 cm^2.

Table 1: Deposition process parameters for the study of the magnetic field strength [6].

Φ (mT)	Peak current (A)	Peak current density ($A.cm^{-2}$)	Voltage (V)	Peak power (kW)	Peak power density ($kW.cm^{-2}$)
22	73	1.22	629	45.92	0.76
26	78	1.29	608	47.10	0.78
30	86	1.43	540	46.44	0.77
35	92	1.53	526	48.39	0.80
44	103	1.72	476	49.03	0.81

Table 2: Deposition process parameters for the study of the magnetic field strength (Paper II).

Φ (mT)	Voltage (V)	Current (A)	Current density ($A. cm^{-2}$)	Pd ($W.cm^{-2}$)
22	490	1.28	0.021	10.16
26	462	1.34	0.022	9.58
30	431	1.45	0.024	8.93
35	419	1.50	0.025	8.69
44	382	1.64	0.027	7.92

The magnetic field flux density was set by moving the magnets plate and measured using a Tesla meter (FM 210 - Projekt Elektronik GmbH, Germany) at the position where the magnetic field strength is maximum. For instance, when the sinus of the angle between the electric field and the magnetic field is equal to 1, i.e. the vectorial product E x B sin(E,B) is equal to E x B, where E is the electric field and B the magnetic field, which is above the middle of the racetrack at the surface of the target. By moving the magnets plate relative to the target, through a knob placed at the back of the magnetron, the magnetic field strength Φ could be controlled. The magnet pack is moved 1.85 cm away from the target to its weakest configuration and an aluminum plate of 0.5 cm is used to help decrease the magnetic field down to 22 mT. The lowest magnetic flux density was 22 mT and the highest 44 mT. A simulation of the magnetic field flux density at these two extrema is shown in Figure 15.

All depositions were made using the same pulse configuration. The frequency was 500 Hz, so the total period (on-time + off-time) was 2000 µs. The pulsing sequence was 6 pulses of 65 µs each. This gives a total on-time of 6*65 µs = 390 µs and a duty cycle of 19.5 %. (390 µs divided by 2000 µs). These conditions show an increase of the peak current up to 78 A, which is an operation mode for high ionization discharge. This pulse configuration has been used in other works before as well. It was shown to reduce arcing and lead to more stable deposition conditions [48].

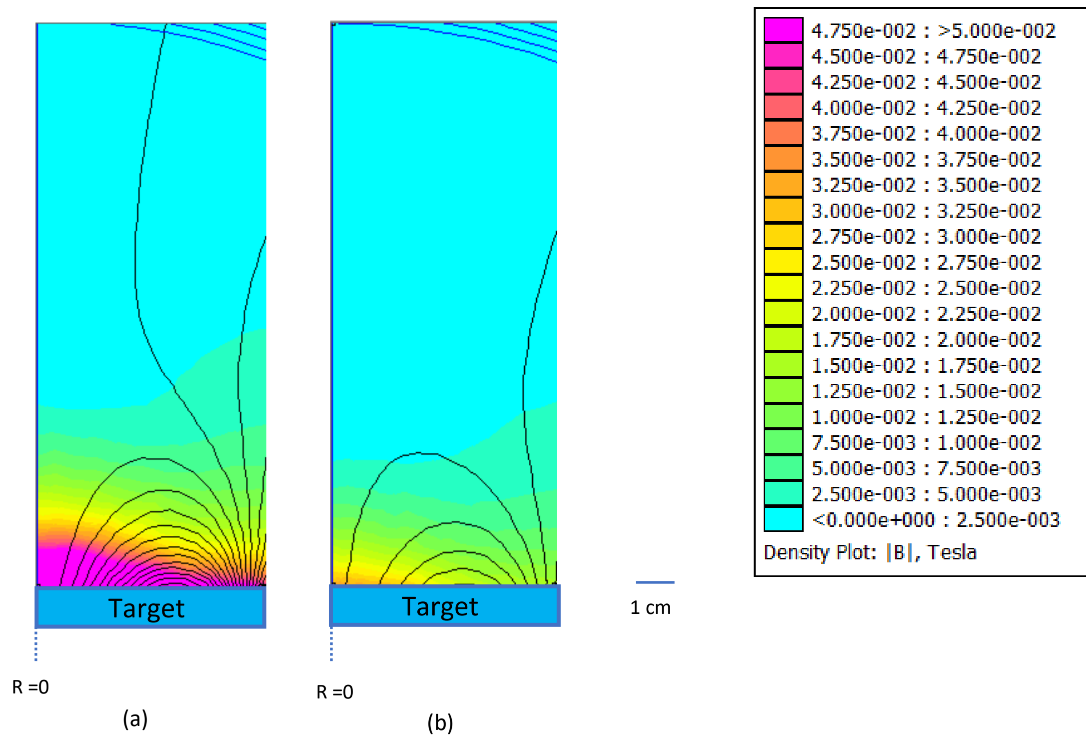

Figure 15: Axisymmetric FEM simulation of magnetic field configuration showing the magnetic field flux density in Tesla; (a): strongest magnetic field, 44mT where the magnets are at a distance of 10 mm from target; (b): weakest magnetic field 22 mT, where the magnets are at a distance of 25 mm from target.

2.2.2. Deposition series at UM6P, Morocco

The results obtained on [49] and [50] were done using the HiPIMS deposition configuration shown in Figure 16 situated at the University Mohammed VI Polytechnique (UM6P). Here the HiPIMS set-up consisted of a DC power supply (GX-ADL GmbH, Germany) connected to the target via a pulsing unit (SPIK3000A-MELEC GmbH, Germany) also used for the dcMS depositions. The size of the vacuum chamber is 56 x 70 x 95 cm^3. The target and the substrate were placed parallel to each other at a distance of 8 cm. The average power was kept constant at a value of 3 kW for all depositions.

The pressure during deposition was measured by a single gauge (TPG 261 A - PFEIFFER Vacuum) and the working pressure was maintained constant at 5 x 10^{-1}Pa using a butterfly valve. The nitrogen and argon flow rate were controlled using mass flow controllers (G-series, MKS, USA).

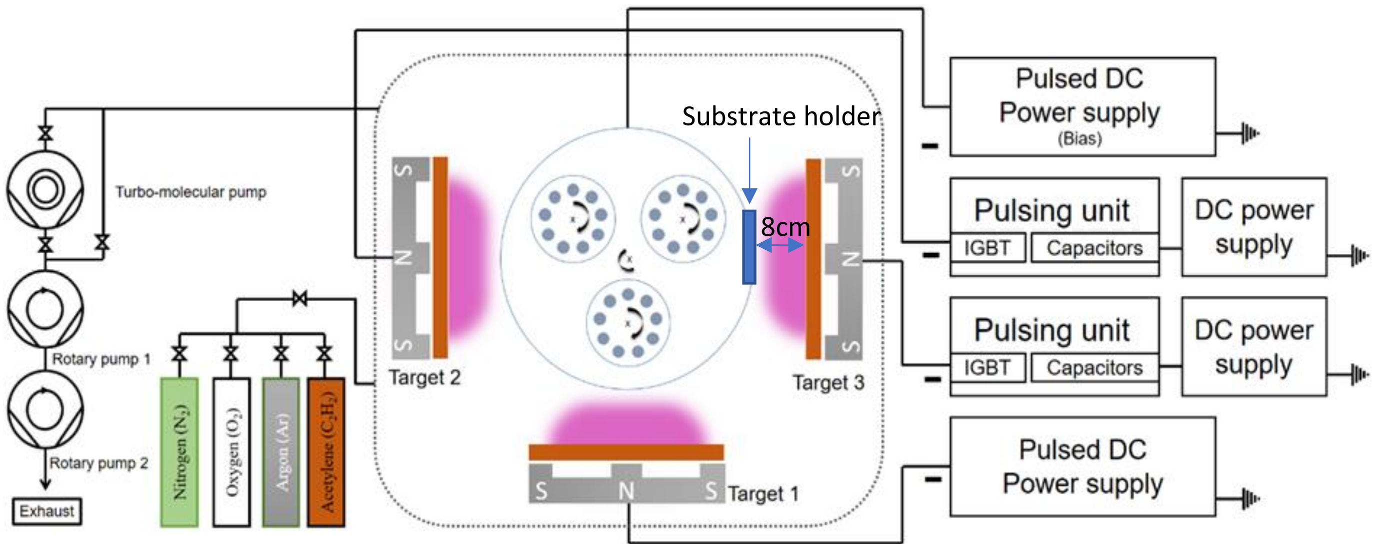

Figure 16: Schematic representation of the magnetron sputtering set-up at the Materials science and Nanoengineering department, MSN, UM6P, Morocco.

The pulsing configuration used in [49] and [50] is shown schematically in Figure 17. A pulse sequence of three pulses of 20 µs on-time separated by 30 µs off-time was used. The pulse period was 1200 µs giving a duty cycle of 5 % and a frequency of 833 Hz. Interrupting a long single pulse by an off time between segments reduces the probability of arcing [48]. Furthermore, the off-time between pulses will decrease the probability of self-sputtering since the ions are allowed to escape from the target during the off-times of the pulse sequence [51]. The 20 µs on-time was chosen because this is the necessary time to detect a significant signal of the sputtered species from the target as shown in previous studies [51]. Moreover, this pulse configuration was found to result in higher deposition rates. The process parameters for HiPIMS deposition are shown in table 3, where the peak current is referring to the average of the three pulses in the pulse sequence. For the reference coating deposited with dcMS, it is shown in table 4.

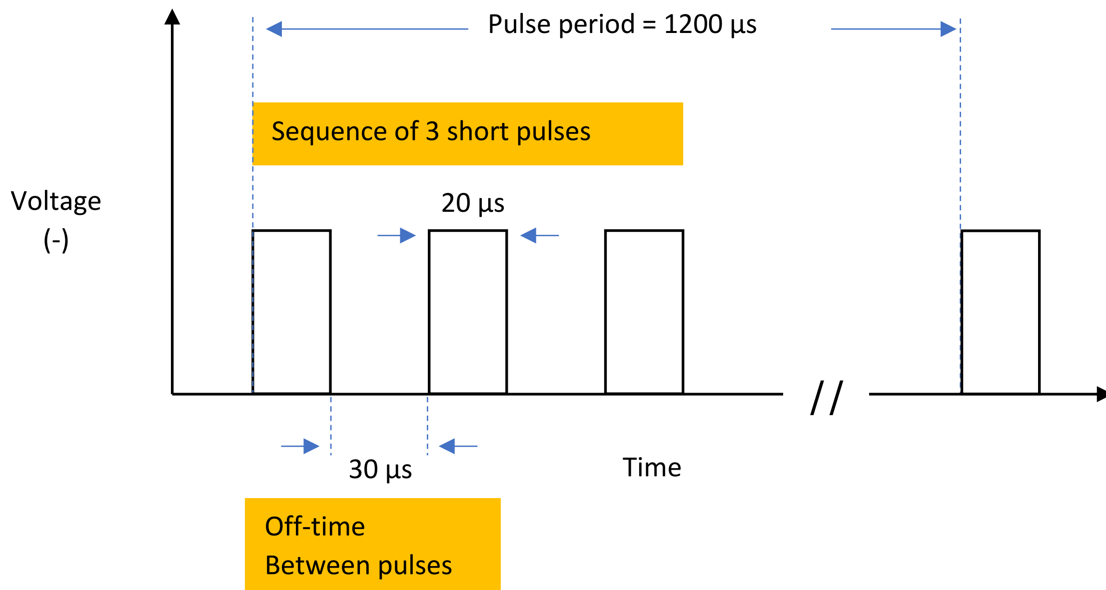

Figure 17: Pulsing configuration used in [49] and [50]

Table 3: Process parameters for each Qv(N2)

$Q_v(N_2)$ (sccm)	$Q_v(Ar)$ (sccm)	U (V)	I_p (A)	J_p ($A.cm^{-2}$)	P_{peak} (kW)	P_{dpeak} ($kW.cm^{-2}$)	Pressure (Pa)	$P_{average}$ (kW)	frequency (Hz)	Duty time (%)
0	**50**	673	169	0.43	113.74	0.29	5.10^{-1}	3	833	5
2	**50**	762	142	0.36	108.20	0.27	5.10^{-1}	3	833	5
3	**50**	752	146	0.37	109.79	0.28	5.10^{-1}	3	833	5
4	**50**	755	147	0.37	110.99	0.28	5.10^{-1}	3	833	5
5	**50**	737	158	0.40	116.45	0.29	5.10^{-1}	3	833	5
6	**50**	732	160	0.40	117.12	0.29	5.10^{-1}	3	833	5

Table 4: Process parameters for the reference coating deposited with dcMS

$Q_v(N_2)$ (sccm)	$Q_v(Ar)$ (sccm)	U (V)	I_p (A)	J_p ($A.cm^{-2}$)	$P_{average}$ (kW)	P_d ($W.cm^{-2}$)	Pressure (Pa)
5	**50**	383	7.8	0.02	3	7.52	5.10^{-1}

3. Thin film characterization

3.1. Mechanical properties (Nano-indentation)

The elastic modulus and hardness of the coatings were extracted from load-displacement measurements determined using Nano-indentation. In conventional indentation hardness tests, the depth of penetration induced beneath the specimen surface is measured as the load is applied to the indenter [52]. The higher the load required producing indentation and the lower the penetration depth induced, the harder the material. Using the size of the area of contact between the indenter and the sample surface, which depends on the penetration depth, the hardness is determined. The area of contact is determined considering the geometry of the indenter. Figure 18 shows the geometry of the different indenters existing [52].

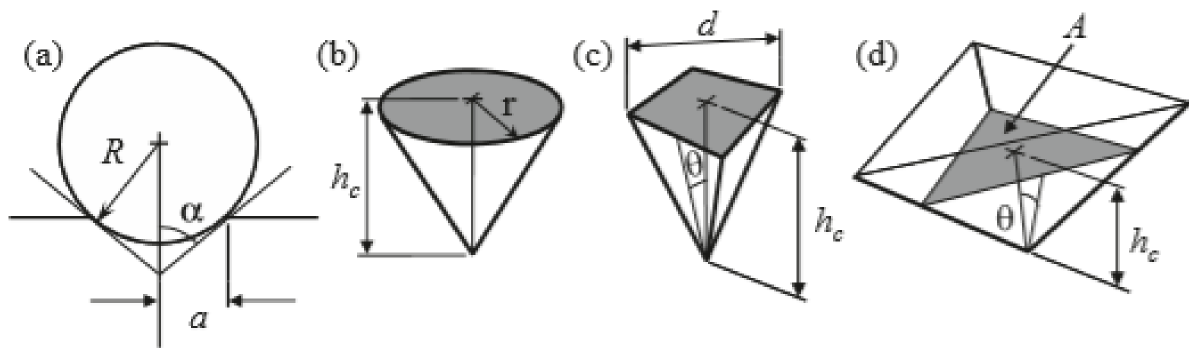

Figure 18: Indentation geometry and parameters for (a) spherical, (b) conical, (c) Vickers, and (d) Berkovich type. The parameter h_c designates the contact depth of the intender penetration.

For nanoindentation testing, it is the Berkovich indenter that is usually used because it is more easily shaped to a sharper point than the four-sided Vickers geometry. This ensures a more precise control over the indentation process [52].

The hardness is equal to the load applied divided by the projected area of contact A which is a function of the contact depth of penetration h_c [52].

$$A = 3\sqrt{3}{h_c}^2(\tan\theta)^2 \quad \text{Equation 11}$$

The angle θ is defined in Fig. 18d. For $= 65.27°$, $A = 24.5{h_c}^2$

So, the hardness H is equal to:

$$H = \frac{P}{24.5 h_c^{2}}$$ Equation 12

The nano-indentation is also used to determine the modulus of the specimen material from a measurement of the "stiffness" of the contact, that is, the rate of change of load and depth [52] [53]. The elastic modulus of the specimen that can be determined from the slope of the unloading of the load-displacement response is formally called the "indentation modulus" E_{IT} of the specimen material [52].

Figure 19 shows a typical load displacement curve obtained using nanoindentation and the different indentation parameters that can be extracted from the curve.

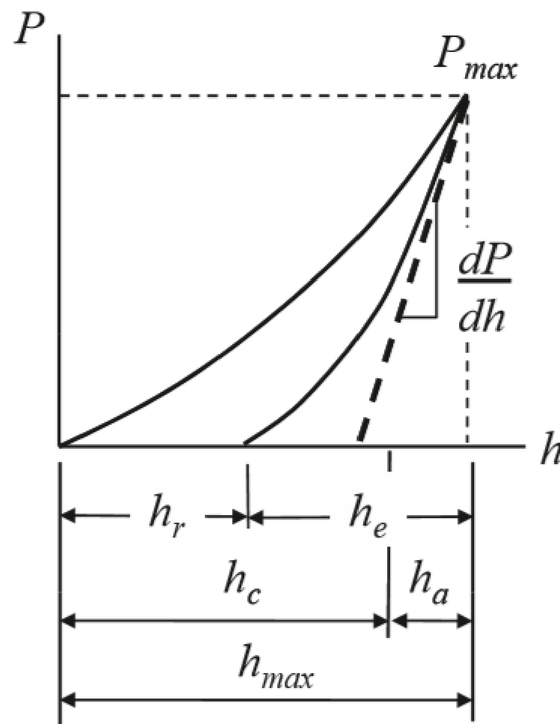

Figure 19: Compliance curves, loading and unloading, from a nanoindentation experiment with maximum load P_{max} and depth beneath the specimen free surface h_{max}. The depth of the contact circle h_c and slope of the elastic unloading dP/dh allow specimen modulus and hardness to be calculated. The h_r is the depth of the residual impression, and h_e is the displacement associated with the elastic recovery during unloading [52].

The relation between E_{IT} and the slope of the unloading curve at maximum load as well as the contact area is given by Equation 13 [52].

$$E_{IT} = \frac{1\sqrt{\pi}}{2\sqrt{A}}\frac{dP}{dh}$$ Equation 13

The relation between the E_{IT} , the Young's modulus of the coating E is given in Equation 13 [53].

$$\frac{1}{E_{IT}} = \frac{1-\vartheta^2}{E} + \frac{1-{\vartheta_i}^2}{E_i}$$ Equation 14

Where ϑ and ϑ_i are the Poisson's ratio of the coating and the indenter respectively, and E_i is the Young's modulus of the indenter material.

For the study of the effect of magnetic field strength (Φ) of the magnetron's magnets on the hardness of TiN [6], the hardness was measured using nano-indentation hardness test (NHT_3, Anton Paar, Germany), using a Berkovich diamond indenter. The indentation load was chosen so that the maximum penetration depth does not exceed 10 % of the coating thickness. The coating thicknesses were on average 1089, 1013, 912, 782, 737 nm for HiPIMS at 22, 26, 30, 35, 44 mT, respectively. The coating thicknesses for dcMS were on average 1073, 1036, 1173, 1240, 1085 nm at 22, 26, 30, 35 and 44mT, respectively. The maximum load of the nano-indentation tests was either 2.5 mN for thicknesses up to 782 nm and 5 mN for thicknesses up to 1089 nm. The loading and unloading rates for a load of 2.5 mN were 5 mN/min, and for a load of 5 mN the loading and unloading rates were 10 mN/min.

For the coatings of 5 µm thickness [49] where the effect nitrogen flow rate is studied, the maximum load was 15 mN and the loading and unloading rate were 30 mN·min^{-1}. The holding time at maximum load was 10 s. The nano-hardness was calculated from an average of at least 16 individual measurements.

3.2. Corrosion resistance

Since corrosion is an electrochemical phenomenon, the kinetics of the surface reactions occurring can be evaluated using electrical methods. The corrosion resistance of a material is often characterized by the corrosion rate which is the loss of metal in unit of length per unit of time. To measure corrosion rate, the polarization measurement is an option. The method that has been used is the Tafel slope extrapolation, which is based on polarization measurement principle [54].

The Tafel slope extrapolation method is based on the fact that the logarithm of the current density varies linearly with the potential of the electrode during an electrochemical reaction [54]. The polarization means that the potential is deviated from equilibrium potential. The equilibrium potential

is obtained by conducting open circuit potential (OCP) i.e. the potential that is obtained when no external current is applied. One distinguishes between two Tafel polarization curves: anodic and cathodic. In anodic polarization where metal oxidation takes place, the potential is shifted to the positive side with respect to the equilibrium potential and for cathodic polarization where reduction of the oxidant from the solution takes place, the potential is shifted to the negative side with respect to the equilibrium potential [54].

The relationship between the applied potential, E_{appl}, and the measured current density, i, in the Tafel region is given by equation 15 for the anodic polarization curve and equation 16 for the cathodic polarization curve.

$$E_{appl} = E_{corr} + \beta_a \log \frac{i_a}{i_{corr}} \qquad \text{Equation 15}$$

$$E_{appl} = E_{corr} - \beta_c \log \frac{i_c}{i_{corr}} \qquad \text{Equation 16}$$

Where β_a and β_c are positive numbers and are called the anodic and cathodic Tafel slopes respectively.

The plots of logarithm of current density (log i) as a function of the applied potential (E) as shown schematically in Figure 20 [1] are called Tafel plots. In the Y-axis, SCE stands for saturated calomel electrode. The corrosion current density, i_{corr}, can be determined according to Equations 15 and 16 by extrapolation of the Tafel lines to $E_{appl} = E_{corr}$, where $i = i_{corr}$ as illustrated in Figure 20.

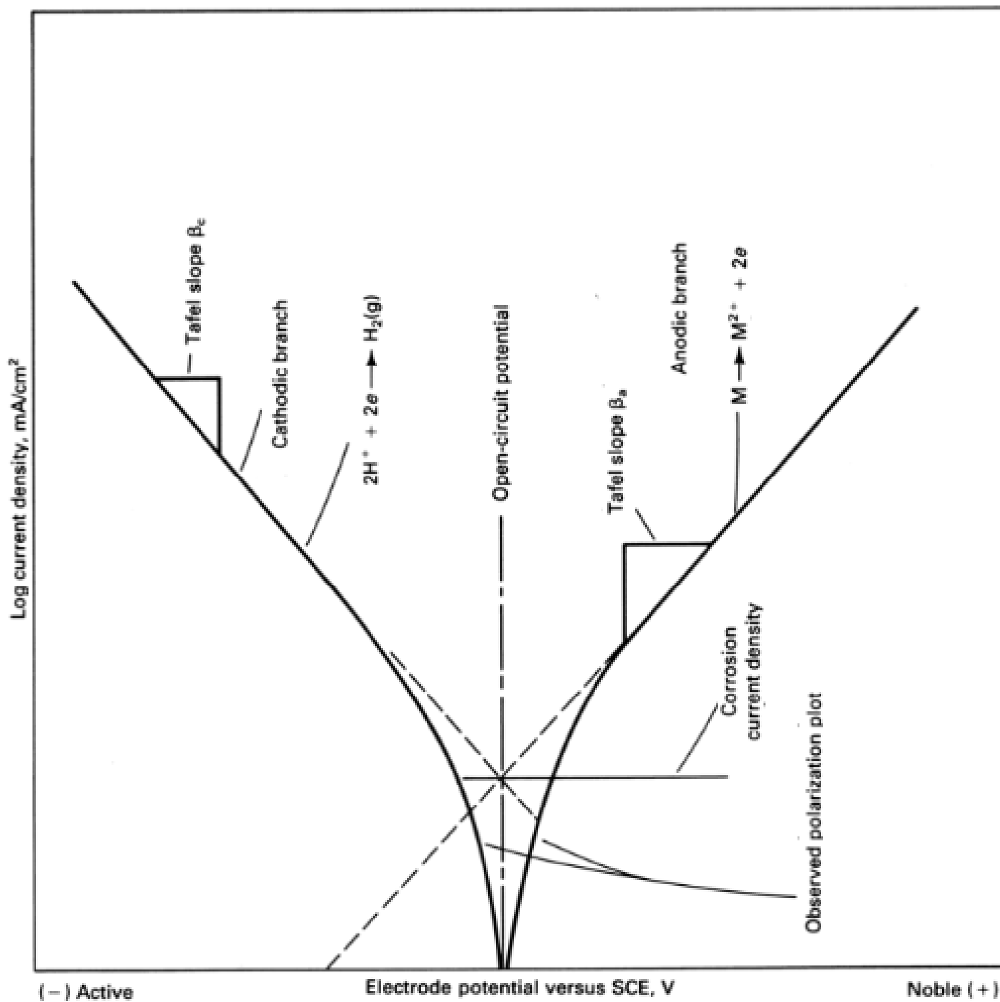

Figure 20: Theoretical Tafel plots illustrating the Tafel extrapolation method. (adapted from reference [1] p:1168).

Another technique that has been used to assess the corrosion resistance of the coatings is the Electrochemical Impedance Spectroscopy (EIS) which is a non-destructive technique that gives accurate kinetic and mechanistic information of a corroding system [54]. The impedance of the system is measured by applying a sinusoidal potential to an electrochemical cell and then the sinusoidal current is measured [54]. The measurement is performed by sweeping the frequency in a defined range and measuring the impedance at each point. The impedance measurement is done by applying small amplitude perturbation signals. In order to determine the cell impedance, the input and output signals are analyzed. The input potential signal is expressed as follows:

$$E_t = E_0 \sin(\omega t) \qquad \text{Equation 17}$$

Where, E_t the oscillating potential at time t, E_0 is the signal amplitude and ω is angular frequency. The angular frequency (ω expressed in radians/second) and the frequency (f expressed in Hertz) are related to each other by the following expression:

$$\omega = 2\pi f \qquad \text{Equation 18}$$

The responding current signal I_t has the different amplitude I_0 and is phase shift (φ), The output current signal is expressed as follows [54]:

$$I_t = I_0 \sin(\omega t + \varphi) \qquad \text{Equation 19}$$

For the calculation of impedance, an expression analogous to Ohm's law is applied which is:

$$Z = \frac{E_t}{I_t} = \frac{E_0 \sin \omega t}{I_0 \sin(\omega t + \varphi)} \qquad \text{Equation 20}$$

One can express the voltage and current in the form of complex function:

$$E_t = E_0 e^{i\omega t} \text{ and } I_t = I_0 e^{-i(\omega t + \varphi)} \qquad \text{Equation 21}$$

Where, i is an imaginary number. According to Ohm's law, the impedance (Z) is related to potential and current signals as follows:

$$Z\ (\omega) = \frac{E_t}{I_t} = |Z|(\cos \varphi + i \sin \varphi) = Z_{real}(\omega) + iZ_{imaginary}(\omega) \qquad \text{Equation 22}$$

The impedance results are presented in the form of Nyquist plot and Bode plots. The Nyquist plot is obtained by plotting in the y-axis the negative of the imaginary part of the impedance and along the x-axis the real part of the impedance. In the Nyquist plot, each point is the impedance at a particular frequency [54]. The region of high frequencies lies in the left side of the Nyquist plot whereas the low frequency lies on the right side. The Nyquist plot is represented schematically in Figure 21. The impedance is presented as an arrow of length $|Z|$. The angle between this arrow and X-axis is known as a phase angle and is represented by $\varphi = \arg Z$. There is one limitation of the Nyquist plot which is that at any point of the curve, the value of frequency is not known [54]. By applying different equivalent circuit models using resistors, capacitors, diffusion element, inductors, the impedance data is interpreted [54]. For the Nyquist representation shown in Figure 21, an equivalent circuit known as the Randle circuit is used. The Randle's circuit consists of a resistor connected to a parallel-connected resistor and capacitor (Figure 22). This circuit is a simple model consisting of electrolyte resistance, charge transfer resistance and double layer capacitance [54].

The second possibility to present EIS data is the Bode plot in which the modulus of impedance, i.e., $|Z|$ versus the log of frequency is plotted as well as the phase angle shift versus log of frequency. The Bode

plots are more informative than the Nyquist plot as it gives the values of frequency during the whole scan [54].

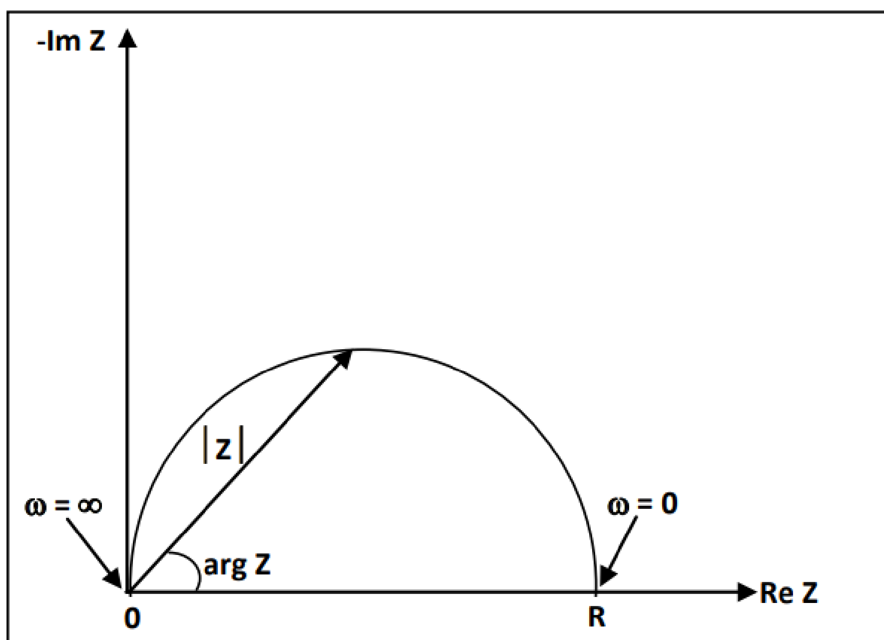

Figure 21: Nyquist plot showing imaginary (–Im Z) and real (Re Z) part of impedance [54].

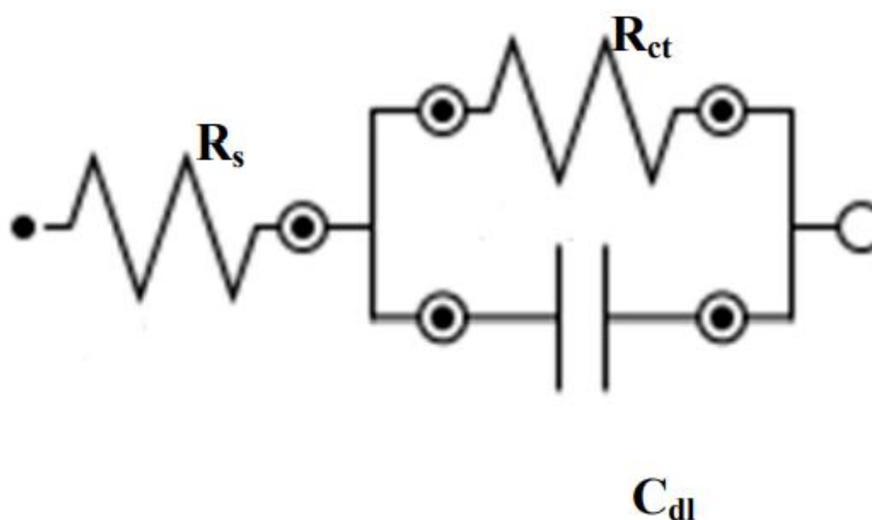

Figure 22: Simple Randle's circuit with one time constant having circuit elements like electrolyte resistance (R_s), charge transfer resistance (R_{ct}) and double layer capacitance (C_{dl}) [54].

For the corrosion tests, potentiodynamic polarization tests (PP) were performed in a three-electrode Teflon® cell at room temperature (20 °C) in phosphoric acid medium. A platinum counter electrode (CE) and a saturated calomel reference electrode (SCE) were used in all electrochemical experiments

performed here by using an SP150 BioLogic potentiostat/galvanostat. The working electrode is the sample which corrosion properties are measured and is the anode. The corrosion potential (OCP) was recorded during 2 h of immersion time and the polarization plots were made with and without coating at a scanning speed of 1 mV.s^{-1}. For the EIS measurement, the initial frequency was scanned from an initial value of 100 kHz to final value of 100 mHz at 10 frequency per decade and amplitude voltage of 10 mV. The experimental set-up is shown in Figure 23. The results of the corrosion tests are presented in [49].

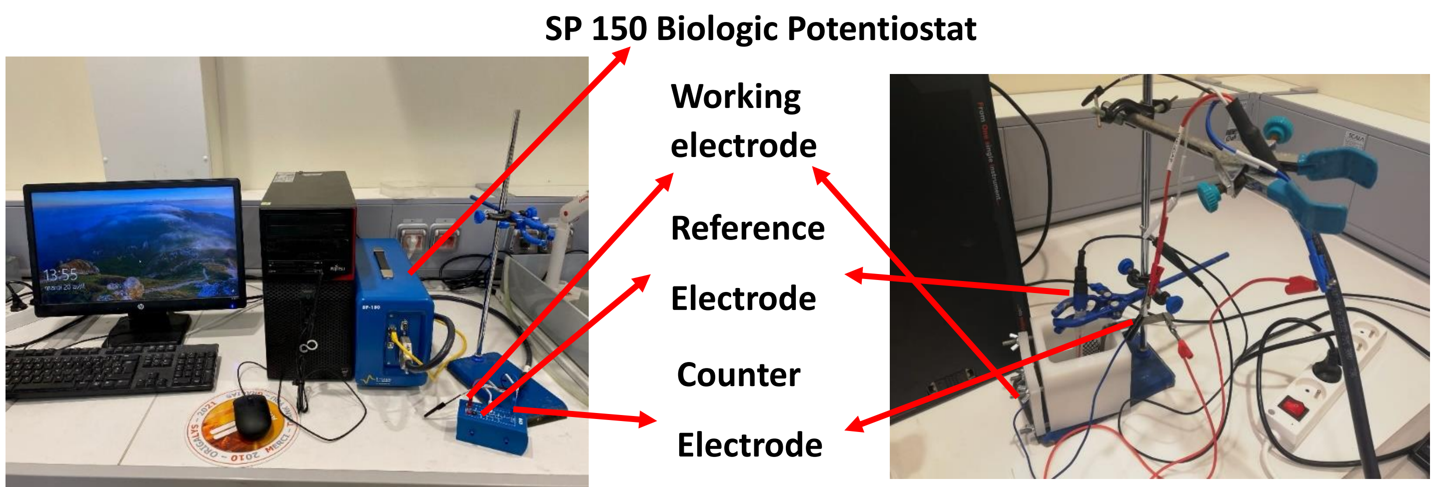

Figure 23: Corrosion test set-up. The working electrode is the sample which corrosion properties are measured and is the anode. The counter electrode is the cathode, and the reference electrode is used to measure the potential of the working electrode.

3.3. Structural analysis

3.3.1. X-ray diffraction (XRD)

XRD is a non-destructive technique, which is used to determine structural properties, such as texture, grain size, residual stress, and lattice parameter. The diffraction of X-rays occurs when their wavelength is in the order of a few angstroms, similar to typical interatomic distances in crystalline solids [55]. X-rays scattered from a crystalline solid can constructively interfere, producing a diffracted beam if the geometric condition for constructive interference is satisfied. This is illustrated in Figure 24 where the path difference between the waves scattered in A and B is equal to:

$$IB + BJ = 2\mathrm{d}\sin\theta \qquad \text{Equation 23}$$

The 'reflected' waves will combine to form a diffracted beam (maximum constructive interference, commonly called 'reflection') if the path difference is a multiple of the wavelength λ.

$$n\lambda = 2\mathrm{d}\sin\theta \qquad \text{Equation 24}$$

Equation 24 is called the Bragg's law [56], where n is an integer, λ is the wavelength, d is the interatomic spacing, and θ is the diffraction angle. For details about the basic principles of X-ray diffraction one can refer to [56] [57].

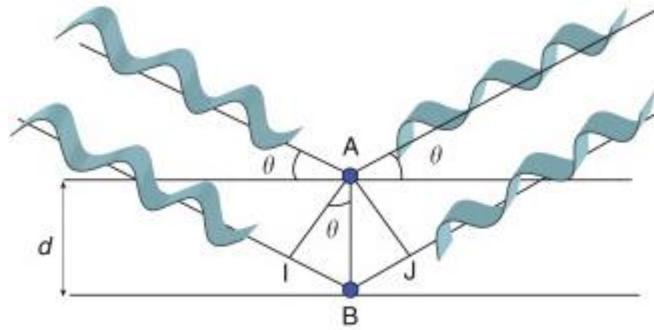

Figure 24: The condition for reflection-the Bragg's law [57].

The XRD diffractograms of the coatings in the present study were detected at room temperature using a D2 Phase diffractometer (Bruker Corp, D8 discover) in the Bragg–Brentano geometry, with Cu Kα radiation (λ=1.5418 Å) at 30 kV and 10 mA.

In this work, the TiN films grown by HiPIMS and dcMS exhibited preferred crystal orientation. The latter was dependent on the deposition process parameters such as magnetic field strength [6] and chemical composition obtained by varying the nitrogen flow rate (paper III). The abundance of the grains that are oriented along a particular (hkl) crystallographic plane with respect to other planes, which determines the most preferred orientation, is given by the texture coefficient according to equation 25 [6]:

$$T_{(hkl)} = \left(\frac{I_{(hkl)}}{\sum I_{(hkl)}}\right) \qquad \text{Equation 25}$$

In which $T_{(hkl)}$ is the texture coefficient, and $I_{(hkl)}$ is the integral intensity of the crystallographic plane from the XRD diffractograms.

Only the crystal orientations that are parallel to the sample surface were detected. In fact, the off-axis angle Ψ as defined in Figure 25 was equal to zero during our measurement which means that the diffraction angle Θ of the (hkl) plane, was equal to the incident angle Ω (see Figure 25) [58]. The symbol σ represents the residual stress which can be extracted from XRD data as explained later in this chapter.

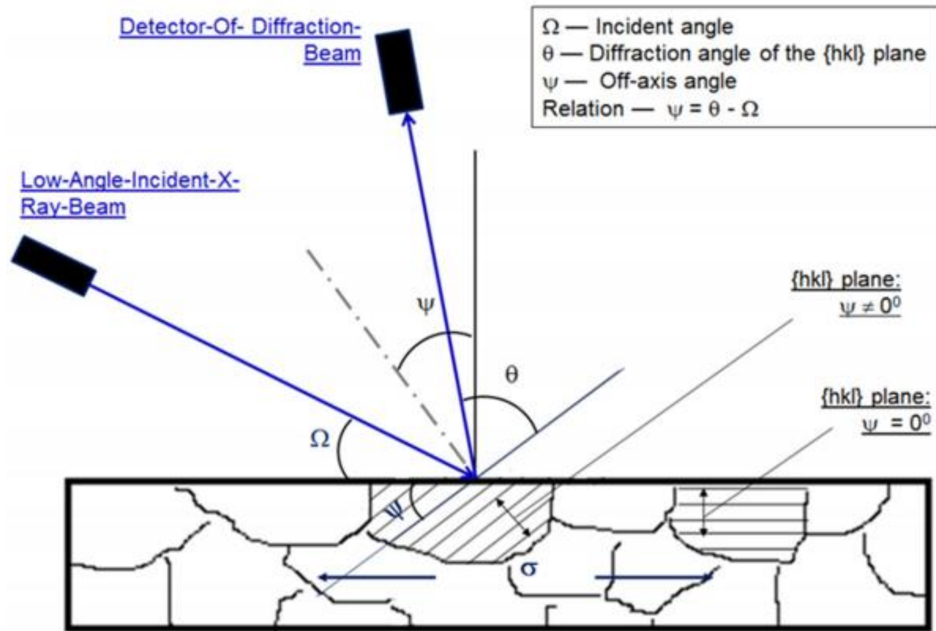

Figure 25: A schematic diagram showing the geometric set-up of X-ray diffraction (XRD) residual stress measurements [58].

The crystal orientation is related to the total energy of the coating W. The coating will grow with the orientation that minimizes this energy [59]. $W_{(hkl)}$ is taken as the summation of surface energy $\gamma_{(hkl)}$ and strain energy $\varepsilon_{(hkl)}$ [59]:

$$W_{(hkl)} = \gamma_{(hkl)} + \varepsilon_{(hkl)} \quad \text{Equation 26}$$

In a study by Pang et al. [60], the static contact angles of water and glycerol on TiN films surface were determined in order to compute the surface energy of the films. The surface energy of the coating was calculated according to equation 27 known as Young's equation [61]:

$$\gamma_S = \gamma_{SL} + \gamma_L \cos\theta \quad \text{Equation 27}$$

The approach used in [60] to determine the surface energy of the solid (the thin film) γ_S was as follows:

- The values of γ_L were known for both the liquids that were used (water and glycerol). The values of θ were measured via the contact angle.
- The approach of Owens and Wendt was used [62] which consist of using the relation of the thermodynamic work of adhesion, defined as the work required to separate two adherent phases to a large distance from each other and is given by Equation 28 [63]:
- $W_{adhesion} = \gamma_S + \gamma_L - \gamma_{SL}$ Equation 28
- $W_{adhesion}$ is then equal to $W_{adhesion} = \gamma_L(1 + \cos\theta)$ Equation 29

- The $W_{adhesion}$ can also be expressed as: $W_{adhesion} = 2\sqrt{\gamma_S{}^d\gamma_L{}^d} + 2\sqrt{\gamma_S{}^p\gamma_L{}^p}$ Equation 30 where $\gamma_S{}^d, \gamma_L{}^d$ are dispersive component of solid and liquid surface energy and $\gamma_S{}^p, \gamma_L{}^p$ are polar component of solid and liquid surface energy.
- Combining equation 29 and 30 lead to: $\gamma_L(1 + \cos\theta) = 2\sqrt{\gamma_S{}^d\gamma_L{}^d} + 2\sqrt{\gamma_S{}^p\gamma_L{}^p}$ Equation 31
- From Equation 30, at least two equations are needed in order to calculate $\gamma_S{}^d$ and $\gamma_S{}^p$ and the final γ_S will be equal to $\gamma_S{}^d$+$\gamma_S{}^p$. To have the two equations, the data of γ_L, $\gamma_L{}^d$ and $\gamma_L{}^p$ of two liquids (here water and glycerol) should be known. These data for water and glycerol are given in reference [60].

The obtained surface energy of TiN films as a function of the thickness is shown in Figure 26 [60]. The ratio of the crystal orientations (111)/(200) is also plotted as a function of the thickness. At a thickness above 1.72 µm, the surface energy shows a drastic decrease which is correlated with a drastic increase in the (111)/(200) ratio as shown in Figure 26, which suggests that the (111) crystal orientation minimizes the surface energy. (200) orientation gives lower strain energy [59].

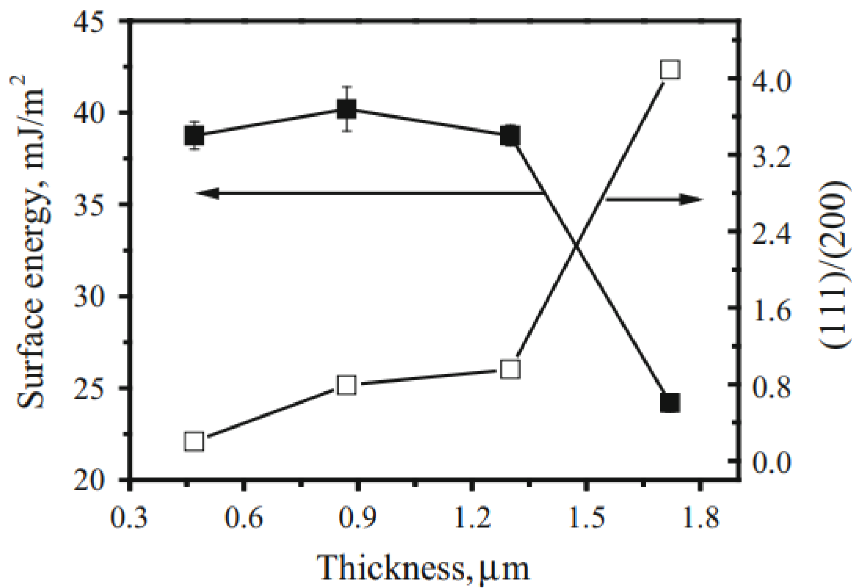

Figure 26: Surface energy and crystal preferred orientation change with the film thickness [60].

Using the nearest-neighbor interaction approximation, the binding energy for one mole of atoms, E_b, in a three-dimensional faced centered cubic (FCC) crystal is given by Equation 32 [60]:

$$\gamma = \frac{E_b}{4N_A}\left(\frac{N}{A}\right) \qquad \text{Equation 32}$$

Where, $\frac{N}{A}$ is the number of atoms per unit area. For the (111) plane $\frac{N}{A_{(111)}} = \frac{4}{a_0{}^2\sqrt{3}}$ which gives:

$$\gamma_{(111)} = \frac{E_b}{N_A a_0{}^2\sqrt{3}} \quad \text{Equation 33}$$

In the case of (200) orientation $\frac{N}{A}_{(200)} = \frac{4}{a_0{}^2}$ which gives:

$$\gamma_{(200)} = \frac{E_b}{N_A a_0{}^2} \quad \text{Equation 34}$$

From equations 33 and 34, it is clear that the surface energy will be lower with (111) orientation than with the (200) preferred orientation which is in coherence with the observed experimental results as shown in figure 26.

In order to estimate the average grain size the Scherrer formula can be used [6] [12] [64] [65]:

$$D = \frac{K\,\lambda}{\beta\cos\theta} \quad \text{Equation 35}$$

Where, D is the average grain size, θ is the diffraction angle, λ is the wavelength of X-rays, and β is the full width at half maximum (FWHM), K is a constant which is equal to 0.9 for cubic thin films [66].

The residual stresses were calculated by estimating the residual strain from the positions of the XRD peaks. Each position of the XRD peak correspond to a lattice spacing as given by the Bragg's formula (equation 24). The out-of-plane residual strain is given by the equation 36 [58] [67]:

$$\varepsilon_{(hkl)} = \left(\frac{d_{(hkl)} - d_{0(hkl)}}{d_{0(hkl)}}\right) \quad \text{Equation 36}$$

Where $d_{(hkl)}$, $d_{0(hkl)}$ are the lattice spacing of stressed and unstressed films, respectively.

According to Poisson formula, the in-plane strain is related to the out-of-plane strain via the Poisson's ratio ϑ as follows: [6]

$$\varepsilon_{(hkl)} = -\vartheta\varepsilon_{biaxial} \quad \text{Equation 37}$$

The biaxial strain $\varepsilon_{biaxial}$ is deduced from Equation 36 and using a weighted average that considers the abundance of the (hkl) crystallographic planes present in the structure:

$$\varepsilon_{biaxial} = -\frac{\sum T_{(hkl)}(\left(\frac{d_{(\mathrm{hkl})} - d_{0(\mathrm{hkl})}}{d_{0(\mathrm{hkl})}}\right))}{\vartheta} \quad \text{Equation 38}$$

Where $T_{(hkl)}$ is the texture coefficient given by Equation 25.

The biaxial stress is then given using the Hook's law as follows:

$$(\sigma_x + \sigma_y) = E\varepsilon_{biaxial} \quad \text{Equation 39}$$

With $\sigma_x = \sigma_y$ assuming an equi-biaxial in plane stress state and considering only planes parallel to the surface where the angle between the diffraction vector and the sample normal is zero [6].

3.3.2. Scanning electron microscopy

The scanning electron microscope (SEM) was used in order to visualize the cross-sectional morphology of the coatings. The SEM has been around for more than 50 years [68]. It involves scanning the sample with a focused beam of electrons along patterns of parallel lines [68]. Signals are then emitted from the specimen when the electrons impinge on it. By detecting the appropriate signals, we obtain the desired image. Figure 27 illustrates schematically the various components of an SEM device [69].

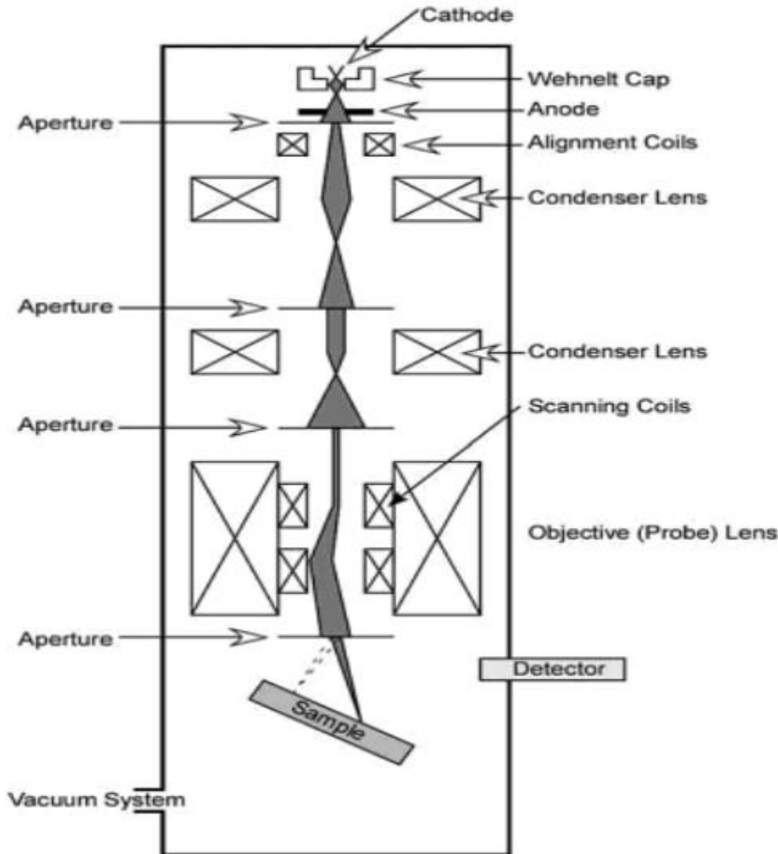

Figure 27: Schematic drawing of the major component of SEM [69].

The electron source, or gun, is situated at the top of the column. Once the electrons are emitted from the negatively charged source, representing the cathode, they move down toward the specimen thanks to a positively charged anode, which is placed after the electron source. Under the influence of

an electric field, the electrons are attracted and accelerated toward the specimen. To focus the electron beam coming from the source into a small probe on the sample surface (diameter of 1 to 50 nm), electromagnetic lenses and apertures are used. Two pairs of scanning coils are used for the scan of the reduced small probe. Once the coils deflect the beam along a line, the coils move the beam to the beginning of the next line where it is deflected once again [69]. The repetition of this process allows an area to be scanned. In order to adjust the roundness of the beam, the stigmators are an important component (not shown in Figure 27). Once the electron beam hits the sample, several signals are generated which are detected by detectors appropriate for each signal. They are then amplified and displayed to obtain an image on the computer screen.

The electrons of the incident beam coming from the source through the electron column are called primary electrons (PEs). When they interact with the specimen, they can undergo multiple elastic and inelastic scattering events. This results into a lateral and vertical spread of the electron beam with respect to the incident direction, and a maximum distance that the electron goes through before its absorption ("penetration depth") [69]. In other words, we have an interaction volume between the electrons and the specimen. It is drawn schematically in Figure 28. Along the penetration depth several signals are generated such as secondary electrons (SE), back scattered electrons (BSE), X-Rays, and less common signals such as Auger electrons. The "escape depth" is the maximum distance that those generated photons and electrons can travel to leave the solid and reach the detector.

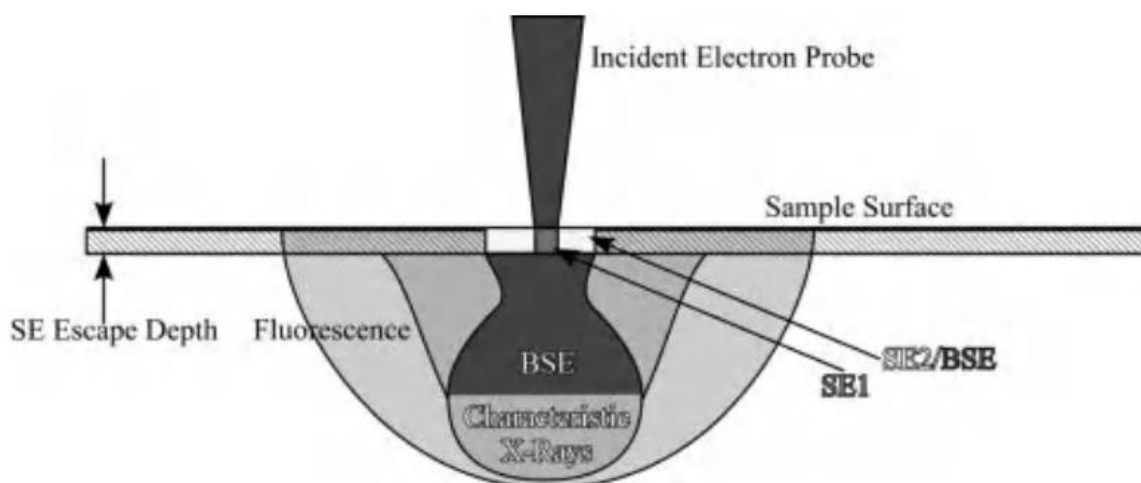

Figure 28: Schematic drawing of the interaction volume and the escape depth for a given material and given energy of the electron beam [69].

In this work, some SEM images of the coating cross-section were obtained using secondary electrons signals. Some of the images are presented in Figure 29 where a comparison between HiPIMS (Figure

29-a) and dcMS (Figure 29-b) is provided showing the morphology of the coating obtained with HiPIMS is featureless whereas for dcMS, the morphology is dense columnar.

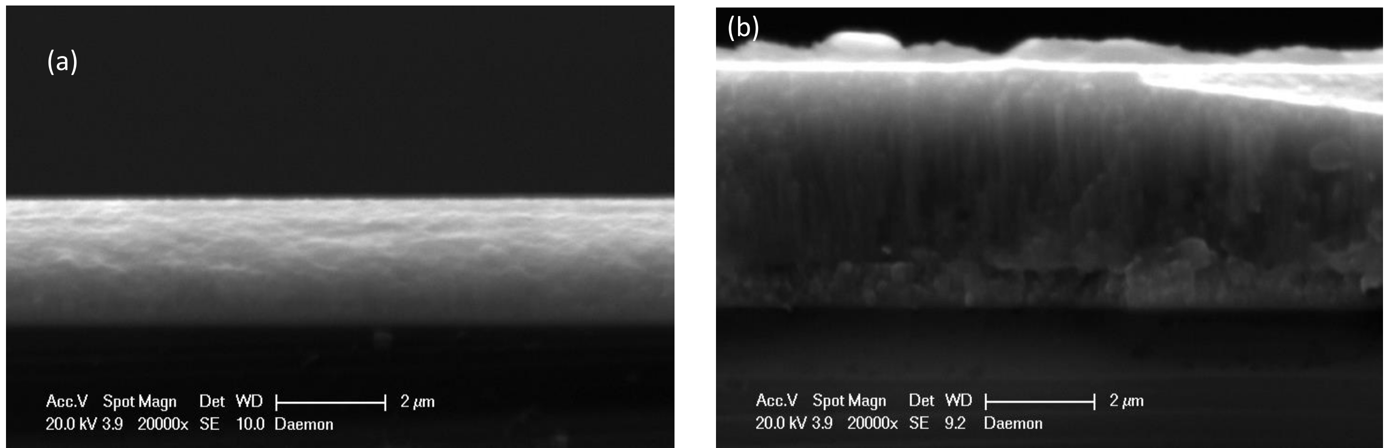

Figure 29: Cross sectional morphology of coating obtained with (a) HiPIMS and (b) dcMS deposited at 50 mT and 1 kW average power.

3.3.3. Atomic force microscopy

The atomic force microscope (AFM) consists of scanning the surface of interest with a very sharp probe. The interactions between the probe and the surface are used to produce a very high-resolution image of the sample, which can reach the sub-nanometer scale depending on the sharpness of the probe tip [70]. The tip is attached to a cantilever that can be bent. By approaching the tip of the cantilevers to the sample surface to a very low distance between them, interaction occur between the atoms. Through these forces, the cantilever is deformed as it scans the surface. To measure the deformation of the cantilever a laser diode sends a laser beam on the back of the cantilever tip and the reflection is monitored with a photodiode which determines the height and torsion deformation of the cantilever. Figure 30 is a schematic representation of the atomic force microscopy device arrangement. The way in which the photodiode detects vertical and horizontal bending of the cantilever is shown in figure 31 [71].

The force-distance curve (Abstandsfunktion) has for two atoms a universal form: the Lennard Jones Potential which function is the sum of the repulsive and attraction potential and it is shown in Figure 32 [72]. The nature of forces that are built between the cantilever tip and the sample surface depend on the distance between them. If the AFM is operated in contact mode, then the potential is in the repulsive interaction domain. If the AFM is conducted in the non-contact mode, then attractive forces

prevail. In this mode the tip oscillates and under the influence of attractive forces, there is a shift in the resonance frequencies. Through the topography of the surface i.e. through different distances between the tip and surface, different resonance shifts are obtained. The Lennard Jones potential is proportional to changes in the frequency and the non-contact mode that is found in attractive domain has the disadvantage that high distances results in small frequency variation. The compromise will be to generate higher frequency variations. This means to come as close as possible to the repulsive domain. This is what is called intermediate mode (between attractive and repulsive domain). This is called tapping mode in which the cantilever oscillates while scanning the surface in close-contact [71].

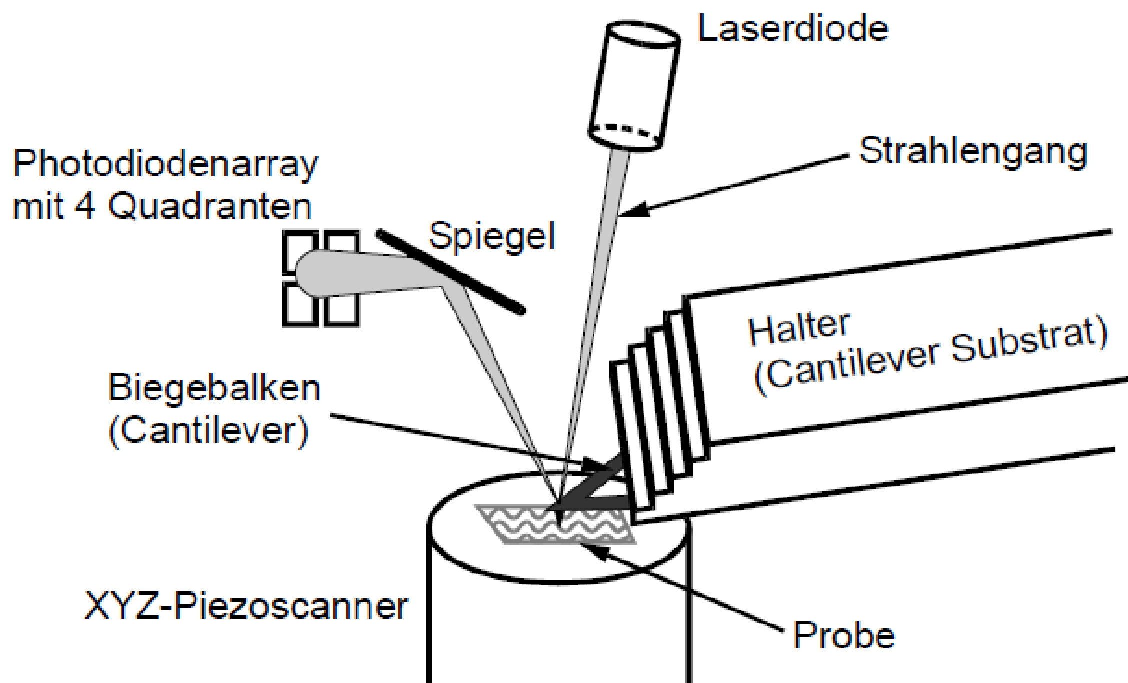

Figure 30: Schematic representation of the set-up of an atomic force microscope. Source: Lecture Prof. Possart, Universität des Saarlandes.

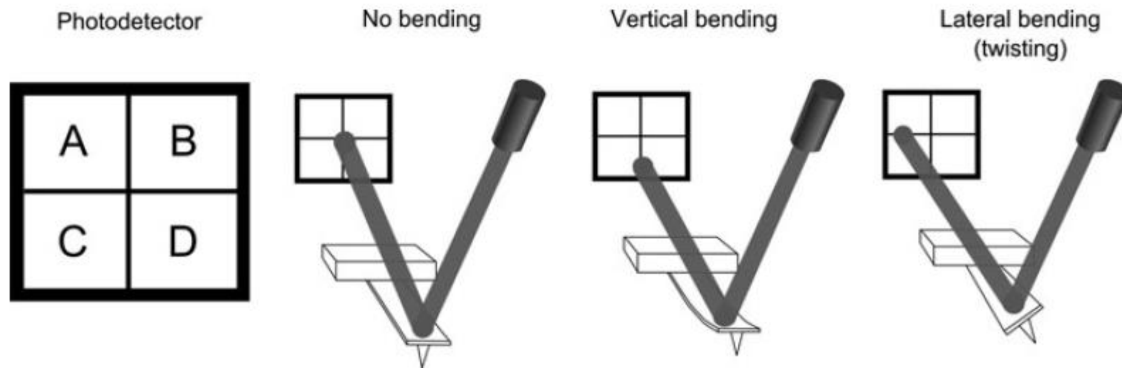

Figure 31: Illustration of how the photodetector detects vertical and horizontal bending of the cantilever [71].

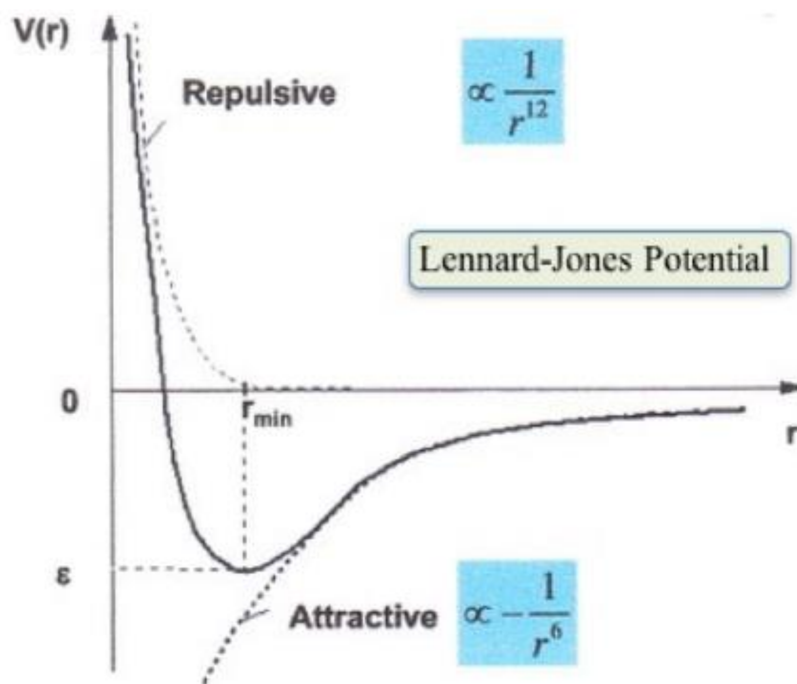

Figure 32: Interaction potentials, Lennard-Jones potential as a function of the particle distance r [72].

3.3.4. Raman spectroscopy

Raman spectroscopy is employed to detect vibrations in molecules based on the Raman scattering process [73]. When materials are subjected to electromagnetic radiation of single frequency, the light would be scattered by the material, both elastically and non-elastically. Elastic scattering occurs when

the scattered light has the same frequency as that of the incoming light. Non-elastic scattering occurs when the scattered light has a different frequency from that of the radiation. Elastic scattering is called Rayleigh scattering, whereas the non-elastic scattering is called Raman scattering [66]. In this work, a DXR 2 Raman Microscope - Thermo Fisher with a laser wavelength of 532 nm was used to measure Raman spectra at room temperature. Samples that were examined were as-deposited and annealed samples at 200°C, 400°C, 500°C, 600°C.

Figure 33 shows the Raman spectra obtained from the surfaces of the TiN coating before and after thermal treatment. All spectra have the same TiN characteristic square-like shape peak at 190-350 cm^{-1}, and a triangular-like shape peak at approximately 555 cm^{-1} for the as-deposited and annealed coatings at temperature of 200°C and 400°C [74,75]. The peaks observed at around 204, 314 and 549 cm^{-1} represent respectively the transverse acoustic mode (TA), longitudinal acoustic mode (LA) and transverse optical mode (TO) in cubic TiN crystals [75–77].

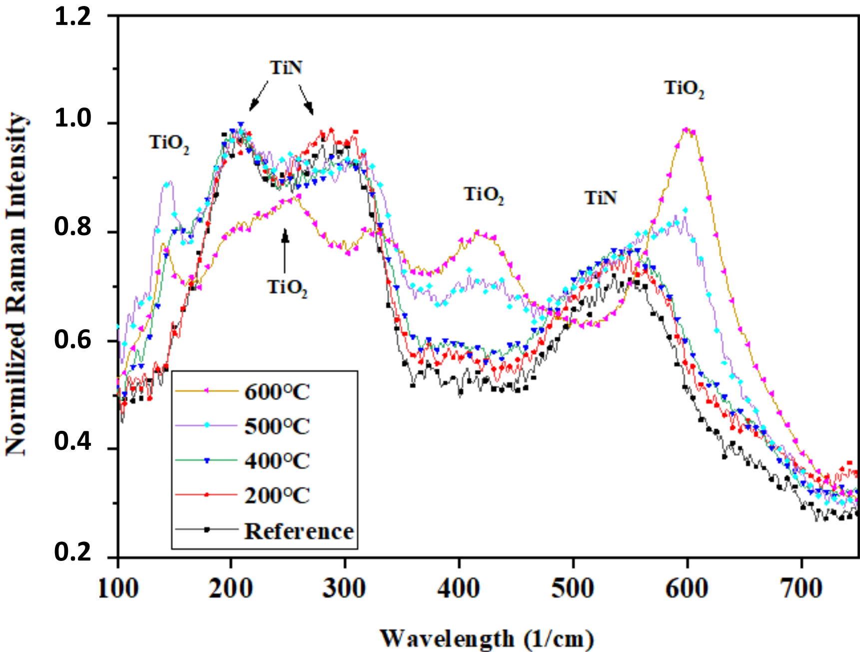

Figure 33: Raman spectra of thin TiN films annealed at different temperatures.

4. Summary of the results

The deposition rate of the HiPIMS process was optimized using the variation of the magnetic field strength Φ parameter. The Φ was set at values of 22mT, 26mT, 30mT, 35mT and 44mT and the deposition rate was measured for TiN coatings grown on steel substrates of Ø40mm x 0.5 mm (which chemical composition is given in paper II, reference [6]). The results are shown in figure 34 a. It is shown that by lowering the Φ, it is possible to deposit coatings in the HiPIMS mode with deposition rate equal to that of dcMS as illustrated in figure 34 b. This concept was explained in the discussion part of reference [6] which content is attached to this thesis.

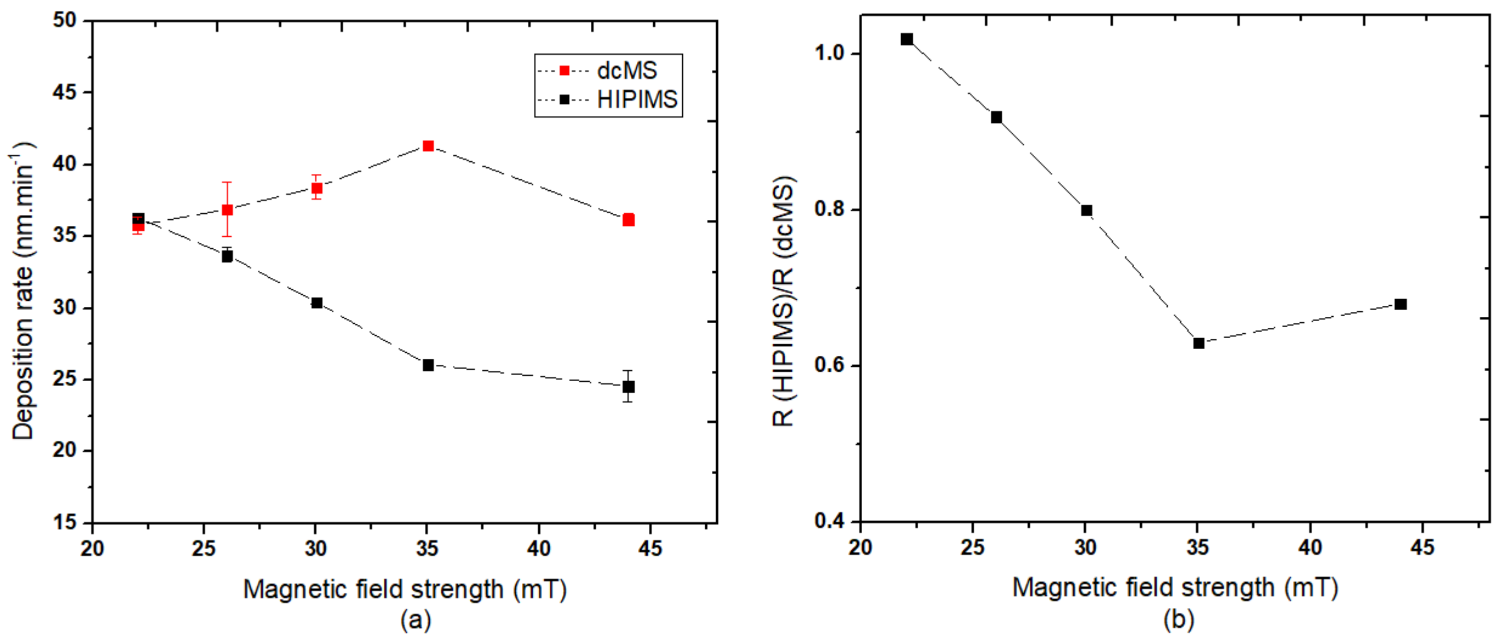

Figure 34: Deposition rate of HiPIMS and dcMS as a function of Φ.

The outcome of Figure 34 is that it is optimal to operate the HiPIMS process at low Φ. However, it is important to see whether low Φ results in acceptable mechanical properties or not. So, the hardness was measured, and the results are shown in Figure 35. The hardness did not show a noticeable variation with the Φ (within the error margin). It is proposed that the considered peak current density interval 1.22-1.72 A·cm^{-2} does not exhibit dramatic changes in the plasma dynamics, which explains the small changes observed for the mechanical properties. However, these results presented in this article are a motivation to further investigate the TiN properties in an even larger peak current density interval [6].

The hardness of the coatings deposited with dcMS was lower than that of the coatings deposited with HiPIMS, which is explained in reference [6]. Nevertheless, the reason why the hardness of the coatings produced with dcMS was high (26 GPa in average over the Φ) was not explained. Therefore, this observation is discussed here:

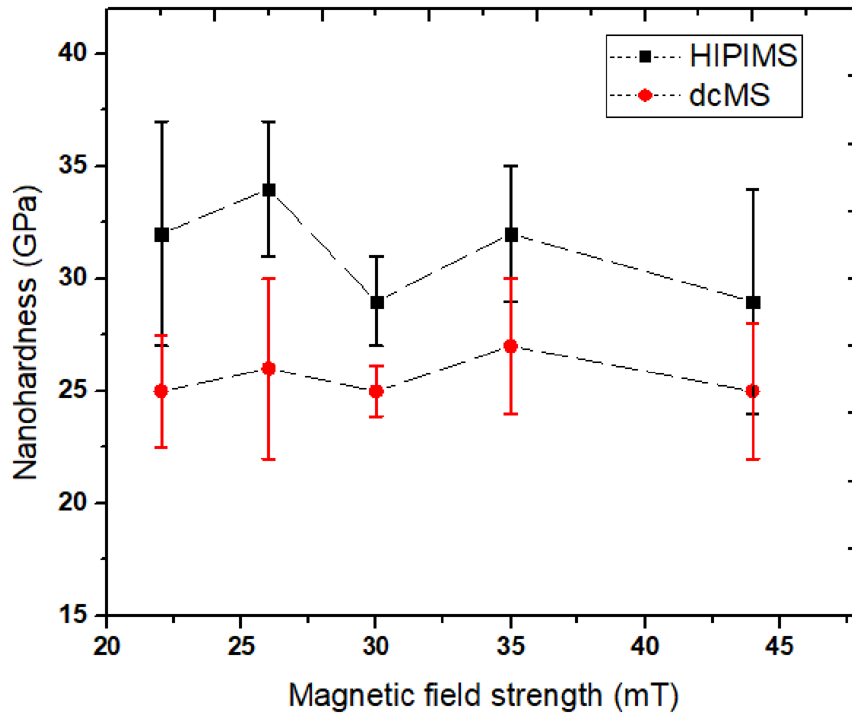

Figure 35: Hardness for coatings obtained with HiPIMS and dcMS as a function of Φ.

In a study by Paulitsch et al. [78], TiN coatings were deposited using unbalanced dcMS and HIPIMS without rotation. It was found that the coatings deposited with dcMS had a hardness of 28GPa, while the hardness measured for coatings deposited with HiPIMS was 39 GPa. It was shown that when moving from static mode (without rotation) to dynamic mode (one-fold substrate rotation), the hardness of TiN coatings deposited with unbalanced dcMS, decreases from 28 GPa to 10 GPa. It was shown that the morphology of the coating deposited with dcMS was strongly influenced if the deposition is conducted in static or dynamic mode. The microstructure was dense with a smooth surface in the static mode while for the dynamic mode it was described as under dense open voided microstructure with rough surface. Therefore, one can conclude according to [78] that the fact that the depositions with the system described in 2.2.1 were performed without rotation has resulted in high hardness (up to 27 GPa) in the case of dcMS. In the case of HiPIMS, as shown in [78], when moving from static to dynamic mode, the hardness only decreased from 38 GPa to 34 GPa.

The microscopic properties of the TiN coatings deposited at different Φ were determined and these are the residual stresses, average grain size, crystal orientation and roughness and were reported and discussed in reference [6] which content is attached at the end of this report.

The optimum setting of Φ with respect to deposition rate and coating properties was determined at NTTF coatings GmbH, Germany (see set-up Figure 14). Further investigations were performed at the University Mohammed VI Polytechnic (see set-up Figure 16). Using this set-up, Ti_xN_{1-x} coatings were produced at low Φ (outcome of reference [6]) and with an optimized pulsing configuration which is shown in Figure 17. The deposition rate (R_d) of Ti_xN_{1-x} coatings produced at different nitrogen flow rate $Q_v(N_2)$ is presented in Figure 36. The R_d decreases gradually with increasing $Q_v(N_2)$. It was possible to deposit close-to-stoichiometry TiN coatings in the transition zone at $Q_v(N_2)$=3sccm, 4sccm and 5sccm, at a comparatively (compared to dcMS) high deposition rates. In fact, according to figure 36, the abrupt decrease of deposition rate at the working point, usually observed in reactive sputtering, was not observed in this case [49]. The current and voltage were plotted with increasing and decreasing $Q_v(N_2)$, and the observed hysteresis obtained was low. This is highlighted paper III [49] which content is attached to this report.

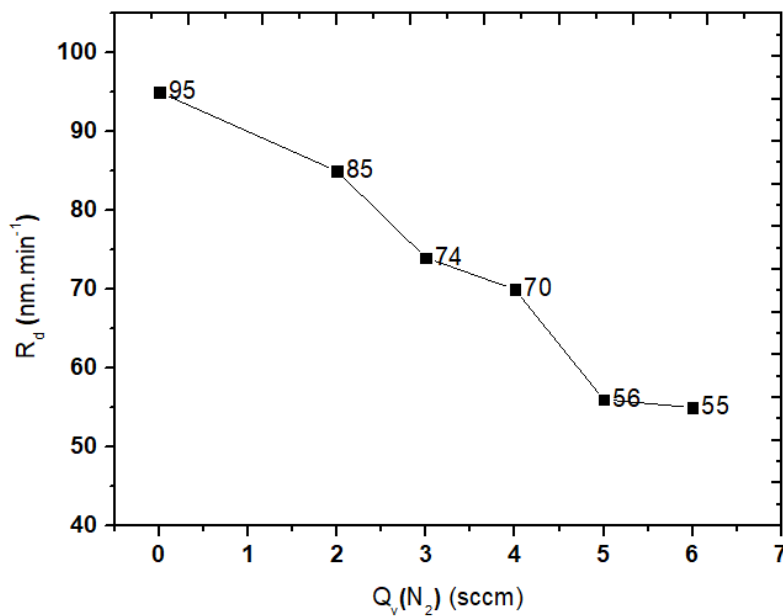

Figure 36: Deposition rate vs $Q_v(N_2)$.

The variation in hardness with respect to $Q_v(N_2)$ is shown in Figure 37 a. It is noticed that a maximum of 28 GPa is achieved at 4sccm, corresponding to 7% in the N_2 fraction. This value can be compared to the TiN coating deposited using deep oscillation magnetron sputtering [79] where a maximum hardness of 16.6 GPa was

reached at N_2 fraction of 6%. Chang et al. [80] reported a maximum hardness of 29.3 GPa reached for stoichiometric TiN at a duty cycle of 5% similar to the duty cycle used in this study.

The maximum young's modulus is at 5sccm according to figure 37.a, and the ratio Hardness/young's modulus (H/E) was maximum at 3sccm as seen in Figure 37 b. This suggests that the coating deposited at 3sccm exhibits more resistance to wear [12]. This is explained by Griffith's theory of fracture that stipulates that the fracture toughness is enhanced with increasing H/E ratio [81].

The abundance of (200) orientation at 4sccm (7% N_2 fraction) (see figure 5 in [49]) proposes that hardness is optimized for this orientation as the Schmidt factor is zero for all slip systems at (200) orientation [6]. When depositing with deep oscillation magnetron sputtering the coating with the highest hardness (6% N2 fraction) had the highest intensity of (200) crystal orientation [79]. Similarly, in our case, the coating with the highest hardness (7% N2 fraction) had also the highest intensity of (200) crystal orientation.

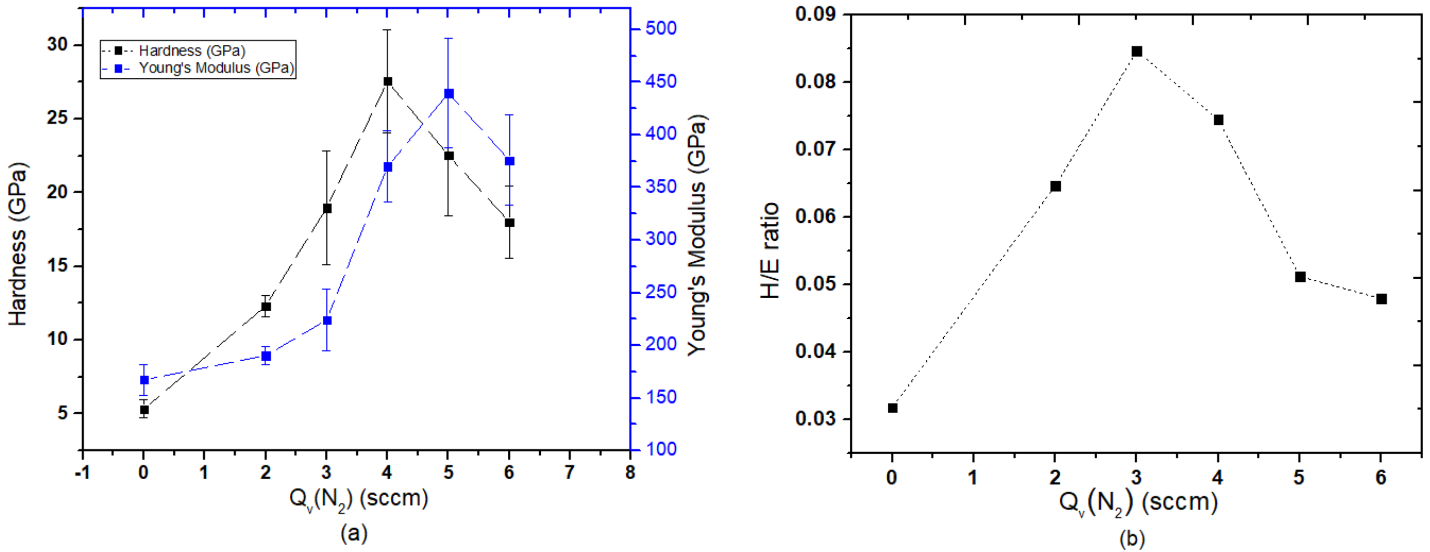

Figure 37: (a) Hardness and Young's Modulus vs $Q_v(N_2)$, (b) H/E ratio as a function of $Q_v(N_2)$.

The results of adhesion properties and coefficient of friction as well as the results on crystal orientation, average grain size, lattice constant, chemical composition are reported and discussed in [49].

The corrosion tests were also conducted on Ti_xN_{1-x} coatings. The Tafel plots obtained from potentiodynamic polarization tests in a 0.1 M phosphoric acid medium are shown in Figure 38. Table 5 contains values of corrosion current density I_{corr}, and corrosion potential E_{corr} as well as corrosion rates. It is observed that all HiPIMS coatings have a low corrosion current density in the range of 0.186-1.464 $\mu A.cm^{-2}$, with the lowest corrosion current density obtained for the TiN coating deposited at 2sccm. The

corrosion current density is proportional to the corrosion rate [82], with a low I_{corr} giving a low corrosion rate. It is known that a high E_{corr} value is an indication of low thermodynamic tendency of the material to corrode [83]. The samples presented in this study show that the highest corrosion potential and the lowest corrosion current density were obtained at 2sccm. All HiPIMS coatings show a very good protection efficiency with values between 91.3-98.9%. For comparison the TiN coating deposited using dcMS showed a low protection efficiency of 50%. The results obtained are discussed in [49].

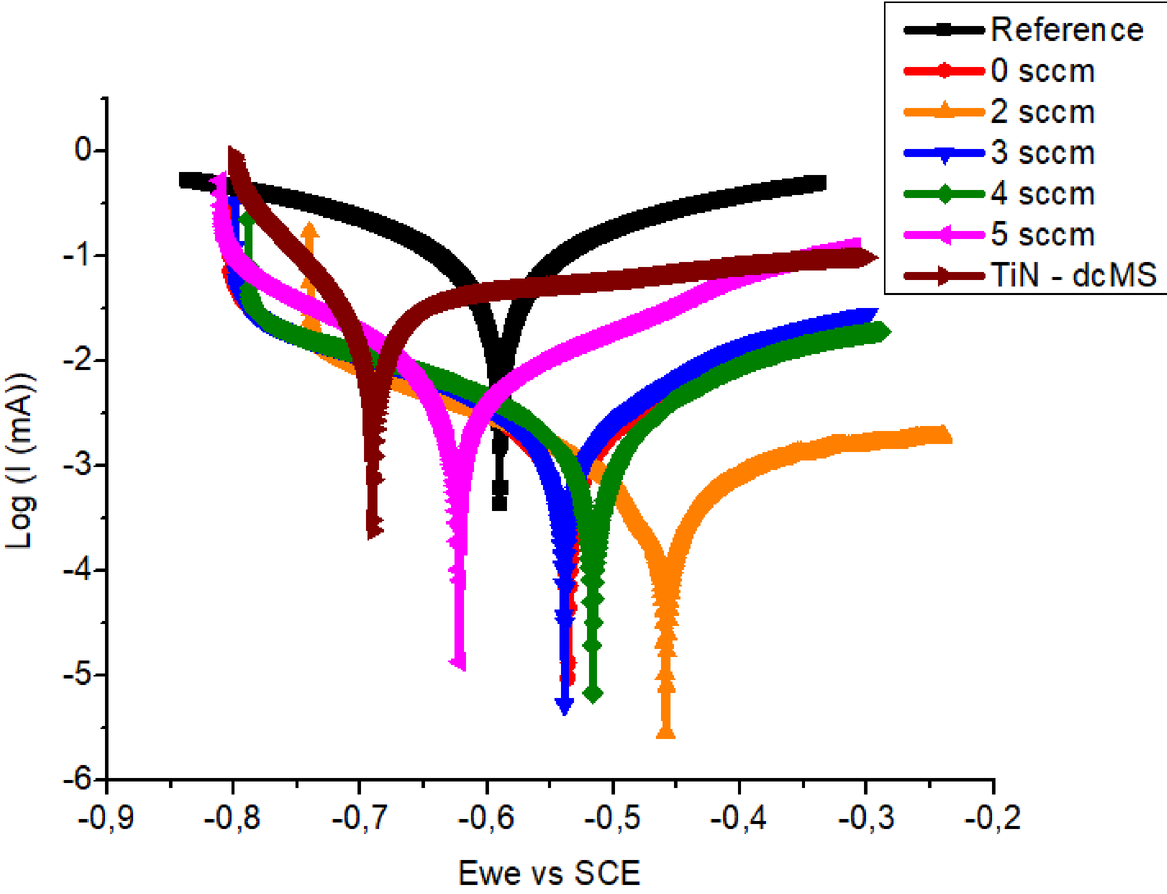

Figure 38: Polarization curves at different $Q_v(N_2)$.

The EIS measurements were also carried out and are presented in figure 39. The detailed description of these results as well as their discussion are presented in [49]. The electrical circuit equivalent to the electrochemical behavior of the samples were also analyzed in [49] attached at the end of this report.

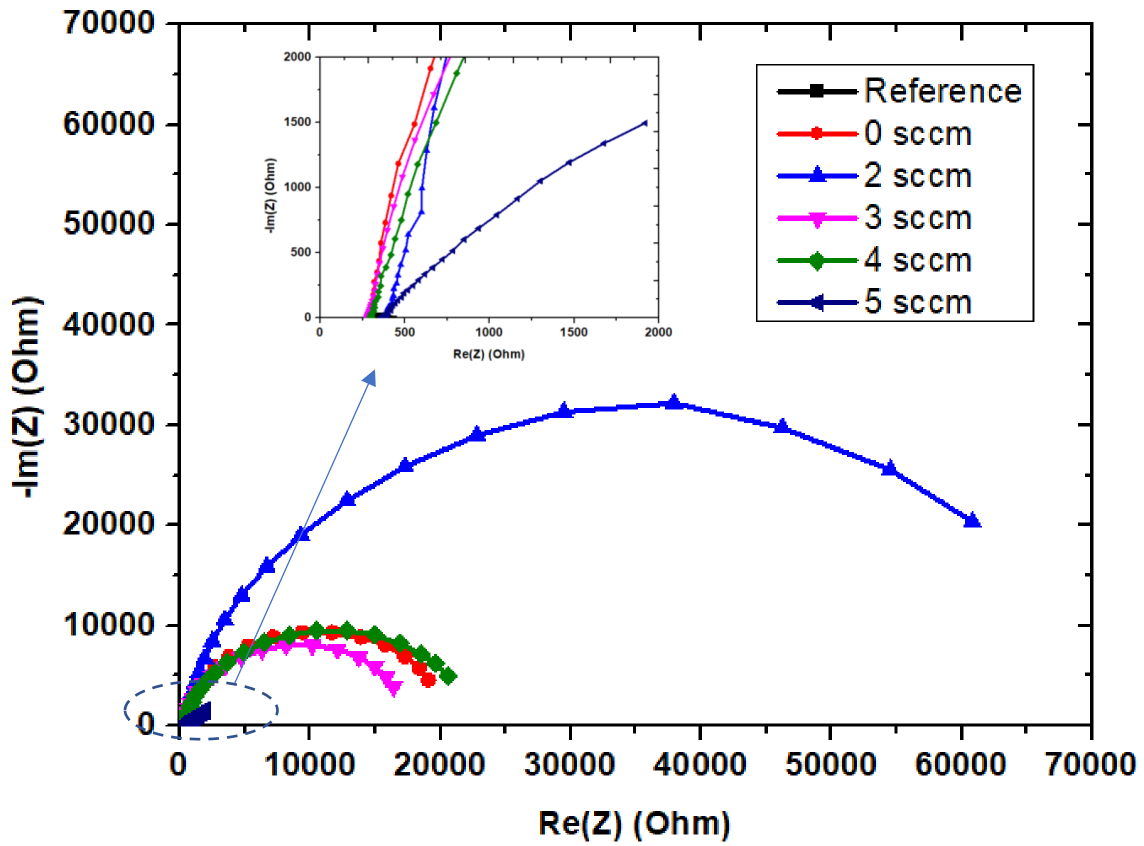

Figure 39: Nyquist plot of coated and uncoated samples at different $Q_v(N_2)$.

Table 5: Corrosion parameters of the reference and the coated steel samples

Sample	**Reference**	**Ti-0sccm**	**TiN-2sccm**	**TiN-3sccm**	**TiN-4sccm**	**TiN-5sccm**	**TiN-dcMS**
E_{corr}(mV)	-591	-535	-459	-540	-515	-623	-691
I_{corr}(μA.cm^{-2})	16.812	0.584	0.186	0.553	0.47	1.464	8.326
Corrosion Rate (mm/year)	0.409	0.014	0.005	0.013	0.011	0.036	0.203
Protection efficiency (%)		96.53	98.89	96.71	97.20	91.29	50.48

The effect of annealing on the mechanical properties of TiN coatings prepared with HiPIMS was also investigated. The results are shown in Table 6.

Table 6: The hardness and Young Modulus for as-deposited and annealed TiN films at different temperatures

Property	As- deposited	200°C	400°C	500°C	600°C
Hardness [GPa]	16.4±1.7	18.7±1.1	21.8±3.0	15.6±0.9	14.1±1.0
Young modulus [GPa]	256±13	251±14	254±28	251±16	223±18

One can see from Table 6 that the hardness obtained here [50] is lower than the hardness obtained in [49] despite the use of the same deposition process parameters. This could be related to the adhesion that was low in the case of the samples prepared for annealing as compared to the adhesion obtained for the coatings prepared at different nitrogen flow rates. In fact, the etching procedure (see section 2.1) was not performed in the case of the coatings which properties are shown in Table 6. Ichimura et al. [84] found experimentally that there is a correlation between the parameter that is characteristic of adhesion (critical load) and the hardness of the coating. The hardness was found to be proportional to the critical load [84]. Results about the effect of annealing on the crystal orientation, average grain size, residual stress and roughness are presented in [50] attached to this thesis. The Raman spectroscopy has been used to confirm the oxidation of TiN for annealing temperatures above 400°C.

5. Conclusion and outlook

The aim of this thesis project is to propose a solution and verify its potentiality for the protection of parts against cavitation erosion and corrosion in phosphoric acid medium. For that, TiN coatings were deposited on steel substrates using the HiPIMS technique which is capable of producing coatings with low defect density especially microporosity that is detrimental to corrosion protection as the corrosive agent can penetrate through these pores. First of all, the operating conditions for a deposition rate of HiPIMS that is comparable with that of dcMS process were found. It was observed that low magnetic field strength improves the HiPIMS deposition rate significantly due to a reduction in the back attraction probability, a phenomenon known as self-sputtering.

The experimental verification of the solution proposed for improving the efficiency of the HiPIMS process in terms of deposition rate, which is the lowering of the magnetic field strength has been validated by measuring the effect of the magnetic field strength on the coating properties that were measured using the appropriate equipment explained in this report. The results have shown that for the used experimental conditions of peak current density that result in small changes in the plasma

dynamics, small changes have been observed in the properties of the coatings upon the change in magnetic field strength. These results were published in surface and coating technology and are attached to this thesis. The depositions have been carried out at NTTF coatings GmbH, Germany.

The next work package was conducted at MSN, UM6P Morocco. The output of the previous work was utilized, and the aim was to find out if the chemical composition of TiN will influence corrosion resistance. Therefore, TixN1-x were deposited using HiPIMS by varying the nitrogen flow rate in reactive mode. It was shown that the mechanical properties are strongly influenced by the chemical composition and are maximum for TixN1-x coatings close to stoichiometry, but the corrosion properties did not show a significant change and remain very good. It was concluded that a TixN1-x close to stoichiometry should be selected to bring about corrosion resistance without compromising mechanical properties. The microscopic properties of the coatings were also determined, and the techniques used are explained in this report. The results of this work were published in Applied Surface Science and the paper is attached to this thesis.

With the purpose to determine the thermal stability of TiN coatings, the best chemical composition determined from the previous work package was deposited, the annealing was conducted at different temperatures and the properties of TiN coating were evaluated. It was shown that annealing can improve the mechanical properties and that there is an optimum. The microscopic properties of residual stress, crystal orientation, average grain size and roughness were determined. The Raman spectroscopy has been used to detect the oxidation of the coating. These results have been published in Journal of Materials Engineering and Performance. The paper is attached to this thesis.

Concerning the use of PVD technique in Morocco, it is absent because no companies that are specialized in this domain are implemented in the country. Thus, the industrials like RENAULT, SNOP, GMD, BAMESA, DELPHI, YAZAKI, SEWS, LEAR, STELLANTIS are obliged to export their part abroad to perform PVD surface treatment. This solution is not optimal as other expenses are added such as the transportation fees and the increase of duration of the treatment. To solve this problem, companies of surface treatment using PVD must be installed in the country. This will serve the firms already present in Morocco but will encourage other international ones to come to the country because of the availability of this coating service. The PVD laboratory at MSN UM6P has the ambition to serve the industry in Morocco especially the producers of cutting tools and automotive companies, and OCP, to improve the properties of the surfaces of their products such as mechanical properties, resistance to corrosion and wear.

6. References:

[1] T.A. Adler, D. Aylor, A. Bray, Corrosion: Fundamentals, Testing, and Protection, ASM Int. (2020) 62–69. https://doi.org/10.31399/asm.tb.cpi2.t55030062.

[2] S. Zhang, W. Zhu, TiN coating of tool steels: a review, J. Mater. Process. Tech. 39 (1993) 165–177. https://doi.org/10.1016/0924-0136(93)90016-Y.

[3] T. Goto, C.Y. Guo, H. Takeya, T. Hirai, Coating of titanium carbide films on stainless steel by chemical vapour deposition and their corrosion behaviour in a Br2-O2-Ar atmosphere, J. Mater. Sci. 27 (1992) 233–239. https://doi.org/10.1007/BF02403668.

[4] B. Shi, J. Jia, X. Feng, G. Ma, Y. Wu, B. Cao, Thermal evaporated CuI film thickness-dependent performance of perovskite solar cells, Vacuum. 187 (2021). https://doi.org/10.1016/j.vacuum.2021.110076.

[5] D.O. Meyer, Sputtering by particle bombardment, vol. I: Physical sputtering of single-elements solids, Springer Berlin Heidelberg, ISBN: 3540105212, 1982. https://doi.org/10.1016/0022-3115(82)90441-x.

[6] A. Ghailane, H. Larhlimi, Y. Tamraoui, M. Makha, H. Busch, C.B. Fischer, A. Jones, The effect of magnetic field configuration on structural and mechanical properties of TiN coatings deposited by HiPIMS and dcMS, Surf. Coatings Technol. 404 (2020) 126572. https://doi.org/10.1016/j.surfcoat.2020.126572.

[7] H. Ichimura, F.M. Rodriguez, A. Rodrigo, The composite and film hardness of TiN coatings prepared by cathodic arc evaporation, Surf. Coatings Technol. 127 (2000) 138–143. https://doi.org/10.1016/S0257-8972(00)00563-6.

[8] K.T.K. Chiang, R. Wei, Growth morphology and corrosion resistance of magnetron sputtered Cr films, Surf. Coatings Technol. 206 (2011) 1660–1665. https://doi.org/10.1016/j.surfcoat.2011.09.020.

[9] R.R. Aharonov, M. Chhowalla, S. Dhar, R.P. Fontana, Factors affecting growth defect formation in cathodic arc evaporated coatings, Surf. Coatings Technol. 82 (1996) 334–343. https://doi.org/10.1016/0257-8972(95)02773-4.

[10] A. Ghailane, M. Makha, H. Larhlimi, J. Alami, Design of hard coatings deposited by HiPIMS and dcMS, Mater. Lett. 280 (2020) 128540. https://doi.org/10.1016/j.matlet.2020.128540.

[11] B. Biswas, Y. Purandare, A. Sugumaran, I. Khan, P.E. Hovsepian, Effect of chamber pressure on defect generation and their influence on corrosion and tribological properties of HIPIMS deposited CrN/NbN coatings, Surf. Coatings Technol. 336 (2018) 84–91. https://doi.org/10.1016/j.surfcoat.2017.08.021.

[12] I.L. Velicu, V. Tiron, C. Porosnicu, I. Burducea, N. Lupu, G. Stoian, G. Popa, D. Munteanu, Enhanced properties of tungsten thin films deposited with a novel HiPIMS approach, Appl. Surf. Sci. 424 (2017) 397–406. https://doi.org/10.1016/j.apsusc.2017.01.067.

[13] J. Wu, B.H. Wu, D.L. Ma, D. Xie, Y.P. Wu, C.Z. Chen, Y.T. Li, H. Sun, N. Huang, Y.X. Leng, Effects of magnetic field strength and deposition pressure on the properties of TiN films produced by high power pulsed magnetron sputtering (HPPMS), Surf. Coatings Technol. 315 (2017) 258–267. https://doi.org/10.1016/j.surfcoat.2017.02.051.

[14] J.M.E. Sci, N.S. Patel, J. Menghani, K.B. Pai, M.K. Totlani, Corrosion behavior of Ti 2 N thin films in various corrosive environments, 1 (2010) 34–43. https://www.jmaterenvironsci.com/Document/vol1/5-JMES-04-2010-Patel.pdf

[15] E.O. Hulburt, The preparation of sputtered metal films, Rev. Sci. Instrum. 5 (1934) 85–88. https://doi.org/10.1063/1.1751791.

[16] J.E. Greene, Review Article : Tracing the recorded history of thin-film sputter deposition : From the 1800s to 2017, J. Vac. Sci. Technol, A 35 (2017). https://doi.org/10.1116/1.4998940.

[17] W.D. Westwood, Glow discharge sputtering, Prog. Surf. Sci. 7 (1976) 71–111. https://doi.org/10.1016/0079-6816(76)90002-2.

[18] G.S. Anderson, W.N. Mayer, G.K. Wehner, Sputtering of dielectrics by high-frequency fields, J. Appl. Phys. 33 (1962) 2991–2992. https://doi.org/10.1063/1.1728549.

[19] J.T. Gudmundsson, Physics and technology of magnetron sputtering discharges, Plasma Sources Sci. Technol. 29 (2020). https://doi.org/10.1088/1361-6595/abb7bd.

[20] M. Samuelsson, High power impulse magnetron sputtering under industrial conditions, Licentitate thesis, Department of physics, University of Linköping, Sweden, 2011. http://liu.diva-portal.org/smash/record.jsf?pid=diva2:410578.

[21] A. Anders, Handbook of Plasma Immersion Ion Implantation and Deposition, A Wiley-interscience publication, 2000.

[22] A. Anders, Tutorial: Reactive high power impulse magnetron sputtering (R-HiPIMS), J. Appl.

Phys. 121 (2017) 171101. https://doi.org/10.1063/1.4978350.

[23] Krishna Seshan, Handbook of Thin Film Deposition, Elsevier, ISBN: 978-1-4377-7873-1 2012. https://doi.org/10.1016/c2016-0-03243-6.

[24] D. Lundin, M. Tiberiu, G.J. Tomas, High Power Impulse Magnetron Sputtering. Fundamentals, Technologies, Challenges and Applications, Elsevier, ISBN: 978-0-12-812454-3, 2020.

[25] A.H. Simon, Sputter Processing, in: Handb. Thin Film Depos. Tech. Process. Technol. Third Ed., Third Edit, Elsevier Inc., 2012: pp. 55–88. https://doi.org/10.1016/B978-1-4377-7873-1.00004-8.

[26] D.M. Mattox, Handbook of Physical Vapor Deposition (PVD) Processing, 2009. http://www.elsevier.com/wps/find/bookdescription.cws_home/717814/description#description.

[27] J. Alami, V. Stranak, A.-P. Herrendorf, Z. Hubicka, R. Hippler, Design of magnetic field configuration for controlled discharge properties in highly ionized plasma, Plasma Sources Sci. Technol. 24 (2015) 045016. https://doi.org/10.1088/0963-0252/24/4/045016.

[28] S.M. Rossnagel, Thin film deposition with physical vapor deposition and related technologies, J. Vac. Sci. Technol, A 21 (2003) S74–S87. https://doi.org/10.1116/1.1600450.

[29] P.A. Cormier, A. Balhamri, A.L. Thomann, R. Dussart, N. Semmar, J. Mathias, R. Snyders, S. Konstantinidis, Measuring the energy flux at the substrate position during magnetron sputter deposition processes, J. Appl. Phys. 113 (2013). https://doi.org/10.1063/1.4773103.

[30] I. V. Svadkovski, D.A. Golosov, S.M. Zavatskiy, Characterisation parameters for unbalanced magnetron sputtering systems, Vacuum, 68, (2002), 283-290, 4. https://doi.org/10.1016/S0042-207X(02)00385-8.

[31] P. Kelly, Continual development keeps reactive sputter deposition at the forefront of surface engineering processes, Mater. Technol. 26, 1, (2011) 1–2. https://doi.org/10.1179/175355511X12955247420178.

[32] D.L. Smith, Thin-film deposition: principles and practice, McGraw-Hill, Inc, ISBN 0-07-113913-3 1996.

[33] T. Zehnder, J. Patscheider, Nanocomposite TiC/a-C:H hard coatings deposited by reactive PVD, Surf. Coatings Technol. 133 (2000) 138–144. https://doi.org/10.1016/S0257-8972(00)00888-4.

[34] J.A. Thornton, D.G. Cornog, R.B. Hall, S.P. Shea, J.D. Meakin, Reactive sputtered copper indium

diselenide films for photovoltaic applications, J. Vac. Sci. Technol. 2 (1984) 307–311. https://doi.org/10.1116/1.572589.

[35] K. Strijckmans, R. Schelfhout, D. Depla, Tutorial: Hysteresis during the reactive magnetron sputtering process, J. Appl. Phys. 124 (2018). https://doi.org/10.1063/1.5042084.

[36] J.A. Thornton, Influence of Apparatus Geometry and Deposition Conditions on the Structure and Topography of Thick Sputtered Coatings., J. Vac. Sci. Technol. 11 (1974) 666–670. https://doi.org/10.1116/1.1312732.

[37] J. Jaramillo-Fernandez, Tuning the thermal conductivity of polycrystalline films via multiscale structural defects and strain, PhD thesis, Ecole Centrale Paris, 33 (2015) 1–212.

[38] W.P. Milantjew, S.W. Temko, Plasmaphysik, Teubner Verlagsgesellschaft, Moskau-Leipzig, 1974.

[39] K. Sarakinos, J. Alami, S. Konstantinidis, High power pulsed magnetron sputtering: A review on scientific and engineering state of the art, Surf. Coatings Technol. 204 (2010) 1661–1684. https://doi.org/10.1016/j.surfcoat.2009.11.013.

[40] U. Helmersson, M. Lattemann, J. Bohlmark, A.P. Ehiasarian, J. Tomas, Review Ionized physical vapor deposition (IPVD): A review of technology and applications, Thin Solid Films, 513 (2006) 1–24. https://doi.org/10.1016/j.tsf.2006.03.033.

[41] V. Tiron, I.L. Velicu, O. Vasilovici, G. Popa, Optimization of deposition rate in HiPIMS by controlling the peak target current, J. Phys. D. Appl. Phys. 48 (2015) 495204. https://doi.org/10.1088/0022-3727/48/49/495204.

[42] V. Kouznetsov, K. MacÁk, J.M. Schneider, U. Helmersson, I. Petrov, A novel pulsed magnetron sputter technique utilizing very high target power densities, Surf. Coatings Technol. 122 (1999) 290–293. https://doi.org/10.1016/S0257-8972(99)00292-3.

[43] D.J. Christie, Target material pathways model for high power pulsed magnetron sputtering, J. Vac. Sci. Technol, A 23 (2005) 330–335. https://doi.org/10.1116/1.1865133.

[44] J. Vlček, P. Kudláček, K. Burcalová, J. Musil, J. Vl, K. Burcalová, High-power pulsed sputtering using a magnetron with enhanced plasma confinement, J. Vac. Sci. Technol, A 42 (2014). https://doi.org/10.1116/1.2388954.

[45] J.W. Bradley, A. Mishra, P.J. Kelly, The effect of changing the magnetic field strength on HiPIMS deposition rates, J. Phys. D. Appl. Phys. 48 (2015) 215202.

https://doi.org/10.1088/0022-3727/48/21/215202.

[46] N.W.M. Edward, P. Goswami, Plasma-based treatments of textiles for water repellency, Elsevier Ltd., The Textile Institute Book Series, 2018. https://doi.org/10.1016/B978-0-08-101212-3.00008-3.

[47] J. Alami, Verfahren zur Vorbehandlung einer zu beschichtenden Oberfläche, Patent, Application number: PCT/EP2014/062795, 2013.

[48] R. Bandorf, V. Sittinger, G. Bräuer, High Power Impulse Magnetron Sputtering – HIPIMS, Elsevier LLtd., Comprehensive materials processing 4 (2014), 75–99. https://doi.org/10.1016/B978-0-08-096532-1.00404-0.

[49] A. Ghailane, A. Olayinka, H. Larhlimi, C. Hejjaj, M. Makha, C.B. Fischer, J. Alami, Titanium nitride , Ti X N (1 − X) , coatings deposited by HiPIMS for corrosion resistance and wear protection properties, Appl. Surf. Sci. 574 (2022) 151635. https://doi.org/10.1016/j.apsusc.2021.151635.

[50] A. Ghailane, E.Y. Maadane, A. Barchid, S. Berchane, H.L. Soukayna Badre-Eddine, M.M. Christian B. Fischer, J. Alami, Influence of annealing temperature on the microstructure and hardness of TiN coatings deposited by HiPIMS, J. Mater. Eng. Perform. (2021) https://doi.org/10.1007/s11665-022-06689-5.

[51] O. Antonin, V. Tiron, C. Costin, G. Popa, T.M. Minea, On the HiPIMS benefits of multi-pulse operating mode, J. Phys. D. Appl. Phys. 48 (2015) 15202. https://doi.org/10.1088/0022-3727/48/1/015202.

[52] A.E. Bergles, G.A. Klutke, K.K. Wang, I. Finnie, H.T. Yang, Nanoindentation, Third Edition, Springer, ISBN: 978-1-4419-9872-9, London, 2011.

[53] C.J. Tavares, L. Rebouta, M. Andritschky, S. Ramos, Mechanical characterisation of TiN/ZrN multi-layered coatings, J. Mater. Process. Tech., 92-93 (1999) 177–183.

[54] S.K. Dhawan, H. Bhandari, G. Ruhi, B.M.S. Bisht, P. Sambyal, Corrosion Preventive Materials and Corrosion Testing, CRC Press, 2020. https://doi.org/10.1201/9781315101217.

[55] J. Alami, Plasma Characterization Thin Film Growth and Analysis in Highly Ionized Magnetron Sputtering, PhD thesis, Linköping University, 2005.

[56] G.B. Greenough, X-ray diffraction by polycrystalline materials, J. Mech. Physics. Solids, 4, 3, (1956) p: 207-208,. https://doi.org/10.1016/0022-5096(56)90078-3.

[57] B.D.Cullity, Elements of X-RAY diffraction, ADDISON-WESLEY PUBLISHINGCOMPANY INC, 1978.

[58] Q. Luo, S. Yang, Uncertainty of the X-ray diffraction (XRD) sin 2 Ψtechnique in measuring residual stresses of physical vapor deposition (pvd) hard coatings, Coatings. 7 (2017). https://doi.org/10.3390/coatings7080128.

[59] D.M. Brunette, P. Tengvall, M. Textor, P. Thomsen, Titanium in Medicine Material Science, Surface Science, Engineering, Biological Responses and Medical Applications, ISBN 978-3-642-63119-1, Springer-Verlag Berlin Heidelberg, 2002. https://doi.org/10.1243/0954411021536432.

[60] X. Pang, L. Zhang, H. Yang, K. Gao, A.A. Volinsky, Residual Stress and Surface Energy of Sputtered TiN Films, J. Mater. Eng. Perform. 24 (2015) 1185–1191. https://doi.org/10.1007/s11665-015-1393-5.

[61] C. Sun, S. Lee, W. Hwang, J. Hwang, I. Tang, Y. Fu, Surface Free Energy of Alloy Nitride Coatings Deposited Using Closed Field Unbalanced Magnetron Sputter Ion Plating Magnetron Sample, Materials Transactions, 47 (2006) 2533–2539. https://doi.org/10.2320/matertrans.47.2533.

[62] D.K. Owens, E.I.P. De Nemours, S. Film, Estimation of the Surface Free Energy of Polymers, J. Appl. Polym. Sci. 13 (1969) 1741–1747.

[63] J.F.Lancaster, The use of adhesives for making structural joints, in: Metall. Weld. (Sixth Ed., 1999: pp. 54–84. https://doi.org/10.1533/9781845694869.54.

[64] A.R. Bushroa, R.G. Rahbari, H.H. Masjuki, M.R. Muhamad, Approximation of crystallite size and microstrain via XRD line broadening analysis in TiSiN thin films, Vaccum 86 (2012) 1107–1112. https://doi.org/10.1016/j.vacuum.2011.10.011.

[65] K.P. Khrishnakumar, C.S. Menon, Determination of the thermal activation energy and grain size of iron phthalocyanine thin films, Mater. Lett. (2001) 64–73.

[66] A.O. Oluwatosin, Surface Morphology Characterization: Magnetron Sputtering Of Nanostructured Titanium Carbide Thin Films On Titanium And Its Alloys, PhD thesis, University of Johannesburg, 2020.

[67] G. Abadias, E. Chason, J. Keckes, M. Sebastiani, G.B. Thompson, E. Barthel, G.L. Doll, C.E. Murray, C.H. Stoessel, L. Martinu, Review Article: Stress in thin films and coatings: Current status, challenges, and prospects, J. Vac. Sci. Technol, A Vacuum, Surfaces, Film. 36 (2018) 020801. https://doi.org/10.1116/1.5011790.

[68] A. Bogner, P.H. Jouneau, G. Thollet, D. Basset, C. Gauthier, A history of scanning electron microscopy developments: Towards “wet-STEM” imaging, Micron. 38 (2007) 390–401. https://doi.org/10.1016/j.micron.2006.06.008.

[69] G.Dehm, In-situ Electron Microscopy, Application in physics, Chemistry and Materials Science, First Edition, ISBN: 978-3-527-31973-2, Wiley-VCH Verlag GmbH, (2012).

[70] D. Johnson, Nidal Hilal, W.R. Bowen, Atomic Force Microscopy in Process Engineering An Introduction to AFM for Improved Processes and Products, ISBN–13: 978-1-85617-517-3, First Edition, Elsevier, 2009.

[71] P. Eaton, P. West, Atomic Force Microscopy, ISBN 978–0–19–957045–4, Oxford University Press, 2010. https://doi.org/10.1093/acprof:oso/9780199570454.001.0001.

[72] D.M. Herlach, T. Palberg, I. Klassen, S. Klein, R. Kobold, Overview: Experimental studies of crystal nucleation: Metals and colloids, J. Chem. Phys. 145 (2016). https://doi.org/10.1063/1.4963684.

[73] G. Dent, E. Smith, Modern Raman Spectroscopy – A Practical Approach, John Wiley and Sons, ISBN 0471-49668-5, 2005.

[74] M. Bernard, A. Deneuville, O. Thomas, P. Gergaud, P. Sandstrom, J. Birch, Raman spectra of TiN/AlN superlattices, Thin Solid Films. 380 (2000) 252–255. https://doi.org/10.1016/S0040-6090(00)01531-5.

[75] X. Bai, X. Shi, L. Xu, F. Huang, C. Zheng, L. Xu, B. Li, Q. Wang, Effects of hydrothermal treatment on physicochemical and anticorrosion properties of titanium nitride coating on pure titanium, Appl. Surf. Sci. 507 (2020) 145030. https://doi.org/10.1016/j.apsusc.2019.145030.

[76] S. Kataria, S. Srivastava, P. Kumar, G. Srinivas, J. Khan, D. Sridhar Rao, H.C. Barshilia, Nanocrystalline TiN coatings with improved toughness deposited by pulsing the nitrogen flow rate, Surf. Coat. Tech. 206 (2012) 19-20, 4279 - 4286. https://doi.org/10.1016/j.surfcoat.2012.04.040.

[77] Z.H. Ding, B. Yao, L.X. Qiu, T.Q. Lv, Raman scattering investigation of nanocrystalline δ-TiN x synthesized by solid-state reaction, J. Alloys Compd. 421 (2006) 247–251. https://doi.org/10.1016/j.jallcom.2005.11.017.

[78] J. Paulitsch, P.H. Mayrhofer, W.D. Münz, M. Schenkel, Structure and mechanical properties of CrN/TiN multilayer coatings prepared by a combined HIPIMS/UBMS deposition technique,

Thin Solid Films. 517 (2008) 1239–1244. https://doi.org/10.1016/j.tsf.2008.06.080.

[79] J.C. Oliveira, F. Fernandes, R. Serra, A. Cavaleiro, On the role of the energetic species in TiN thin fi lm growth by reactive deep oscillation magnetron sputtering in Ar / N 2, Thin Solid Films, 645 (2018) 253–264. https://doi.org/10.1016/j.tsf.2017.10.052.

[80] C. Chang, S. Shih, P. Chen, W. Chen, C. Ho, W. Wu, Effect of duty cycles on the deposition and characteristics of high power impulse magnetron sputtering deposited TiN thin fi lms, Surf. Coat. Technol. 259 (2014) 232–237. https://doi.org/10.1016/j.surfcoat.2014.03.011.

[81] A. Leyland, A. Matthews, On the significance of the H / E ratio in wear control : a nanocomposite coating approach to optimised tribological behaviour, Wear. 246 (2000) 1–11.

[82] L. Velasco, J.J. Olaya, S.E. Rodil, Effect of Si addition on the structure and corrosion behavior of NbN thin films deposited by unbalanced magnetron sputtering, Appl. Phys. A Mater. Sci. Process. 122 (2016) 1–10. https://doi.org/10.1007/s00339-016-9639-0.

[83] E.S. Pana, Iulian, Braic, Viorel, Dinu, Mihaela, Massima Mouele, M. Parau, Anca C, Petrik, Leslie F, Braic, In vitro corrosion of titanium nitride and oxynitride-based biocompatible coatings deposited on stainless steel, Coatings, 10 (2020) 710. https://doi.org/10.3390/COATINGS10080710.

[84] H. Ichimura, A. Rodrigo, The correlation of scratch adhesion with composite hardness for TiN coatings, Surf. Coatings Technol. 126 (2000) 152–158. https://doi.org/10.1016/S0257-8972(00)00541-7.

[85] P. Sigurjonsson, P. Larsson, D. Lundin, U. Helmersson, J.T. Gudmundsson, Spatial and temporal variation of plasma parameters in a HiPIMS discharge, Master thesis, University of Iceland, 2006.

7. Scope of the papers

Paper I:

Here, a review of the hard coatings that were deposited using HiPIMS and dcMS is presented. Values of the hardness obtained with both techniques for different hard coating materials are shortly reviewed. The methods for improving the hardness are highlighted, such as alloying, modification of coating architecture, as well as the choice of deposition technique.

Paper II:

In this paper, the effect of the magnetic field strength Φ on the deposition rate as well as the hardness and structural properties of the coating deposited by HiPIMS and dcMS is studied. It is demonstrated that the deposition rate, in the HiPIMS case, increases when lowering the Φ. On the contrast, in the case of dcMS, the deposition rate was decreasing when diminishing the Φ except from 44mT to 35mT. The hardness did not change (within the error margin) in the studied Φ range [22-44mT]. The coatings deposited with dcMS showed high hardness (25-27GPa) although lower than HiPIMS (29-34GPa). The high hardness in dcMS was attributed to the absence of rotation during deposition but also to high power density ($10W.cm^{-2}$) that has led to the hard crystal orientation (200) that lowers the strain energy induced by ion bombardment of the coating. The evolution of texture coefficient, residual stresses, surface roughness, and average grain size with the Φ are also presented and discussed.

Paper III:

In this paper, the effect of $Ti_xN_{(1-x)}$ chemical composition on the properties such as hardness, coefficient of friction, adhesion as well as corrosion properties is studied. The hardness changed significantly with the nitrogen content and showed a maximum at nitrogen flow rate $Q_v(N_2)$=4sccm which corresponded to $Ti_{0.58}$ $N_{0.42}$. The highest toughness represented by the H/E ratio where H is the hardness and E is the Young's modulus, was maximal at $Q_v(N_2)$=3sccm for $Ti_{0.81}N_{0.19}$. The corrosion properties obtained for coatings deposited using HiPIMS were very good with a protection efficiency ranging from 92% to 96% depending on $Q_v(N_2)$. The protection efficiency was only 50% for coatings deposited at 5 sccm for dcMS.

Paper IV:

In this paper the effect of annealing of the as-deposited stoichiometric TiN using HiPIMS is investigated. Titanium nitride (TiN) coatings were deposited on a silicon substrate without additional heating. The TiN films were annealed at temperatures ranging from 200°C to 600°C, and the properties such as the microstructure, morphology and hardness of TiN were investigated using X-ray diffraction, Raman spectroscopy, atomic force microscopy and nano-indentation. The results are compared to the properties of conventional TiN thin films, typically deposited by dcMS or Arc evaporation at around 400°C. It is found that the hardness of the HIPIMS films increases from 16.4 to 21.8 GPa as the annealing temperature increases to 400°C. For higher annealing temperatures, the hardness of the films decreases, which is attributed to the oxidation of TiN.

8. Appendix

1. Sputtering yield calculator:

```
#include <iostream>
#include <cmath>
using namespace std;
double sputtering_yield_p_r (double, double, double, double);//declaring the function sputtering
yield function_projectile_recoil
double sputtering_yield_r_r (double, double, double, double);//declaring the function sputtering
yield  function_projectile_recoil
int main()
{
   double sp_y_Ar; //Declaring the variable sputtering yield of argon ions bombarding titanium target
   double sp_y_Ti; //Declaring the variable sputtering yield of titanium ions bombarding titanium
target
   double E_i=475; //Declaring the initial energy as the target voltage
   double E_m_f_r; //Declaration of energy mass factor variable in case titanium ions hitting titanium
target
   double E_m_f_p; //Declaration of energy mass factor variable in case argon ions hitting titanium
target
   double E_th_p; //Threshold energy projectile-recoil
   double E_th_r; //Threshold energy recoil-recoil
   double m_r=47.9; //Atomic mass recoil
   double m_p=39.948; //Atomic mass projectile
   double U_b=3.333; //Surface binding energy recoil material
   E_m_f_p=(4*m_r*m_p)/((m_r+m_p)*(m_r+m_p));//Relation of the energy transfer mass factor
projectile-recoil
   E_m_f_r=(4*m_r*m_r)/((m_r+m_r)*(m_r+m_r));//Relation of the energy transfer mass factor
recoil-recoil
   cout<<"Energy mass factor projectile:"<<E_m_f_p<<endl;
   cout<<"Energy mass factor recoil:"<<E_m_f_r<<endl;
   E_th_r=(8*U_b)/(pow((m_r/m_r),0.4));
   cout<<"Threshold energy of sputtering recoil-recoil material:"<<E_th_r<<endl;
   if ((m_p/m_r)<0.3)
   {
    E_th_p=U_b/(E_m_f_p*(1-E_m_f_p));
   }
   else {
      E_th_p=(8*U_b)/(pow((m_p/m_r),(2/5)));
      cout<<"Threshold energy of sputtering projectile-recoil:"<<E_th_p<<endl;
   }
sp_y_Ar = sputtering_yield_p_r(E_i, m_r, E_m_f_p, E_th_p);
cout<<"Sputtering yield projectile-recoil is:"<<sp_y_Ar<<endl;//Display sputtering yield Ar
sp_y_Ti = sputtering_yield_r_r(E_i, m_r, E_m_f_r, E_th_r);
cout<<"Sputtering yield recoil-recoil is:"<<sp_y_Ti<<endl;//Display sputtering yield Ti
double Y_Ar=sp_y_Ar;
double Y_Ti=sp_y_Ti;
}
//This function calculates the sputtering yield of the recoil
```

```
double sputtering_yield_p_r (double E_i, double m_r, double E_m_f_p, double E_th_p)
{
  double sputter_y_Ar; //variable in which the sputtering yield is stored
  sputter_y_Ar=6.4*(pow(10,-3))*m_r*(pow(E_m_f_p,(5/3)))*(pow(E_i,0.25))*(pow((1-
(E_th_p/E_i)),3.5));
  return sputter_y_Ar;
}
double sputtering_yield_r_r (double E_i, double m_r, double E_m_f_r, double E_th_r)
{
  double sputter_y_Ti; //variable in which the sputtering yield is stored
  sputter_y_Ti=6.4*(pow(10,-3))*m_r*(pow(E_m_f_r,(5/3)))*(pow(E_i,0.25))*(pow((1-
(E_th_r/E_i)),3.5));
  return sputter_y_Ti;
}
```

2. Project: Spatially resolved Langmuir probe using Arduino

A Langmuir probe is a relatively simple device for measuring various plasma parameters such as electron density, mean electron energy, electron energy distribution function, plasma potential and floating potential [27]. A Langmuir probe is typically constructed of a thin wire that is inserted into the plasma. The wire radius has to be greater than the electron Debye length. The Debye length is the distance over which significant charge separation can occur [85].

The aim of this project is to design a spatially and temporally resolved Langmuir probe. The spatially resolved characteristic was achieved by programming a microprocessor (Arduino) in the DEV C++ programming language. The program is shown below:

```
#include <Stepper.h>
#include <AccelStepper.h>
#include <MultiStepper.h>

 //Declaring variables
long Steps_Per_RevolutionX=200;
long Steps_Per_RevolutionZ=200;
int EnablePinX=6;
int EnablePinZ=7;
int Limit_switchX=8; // This variable is used to give to arduino a signal to home the linear drive in X-
direction
int Limit_switchZ=9; // This variable is used to give to arduino a signal to home the linear drive in Z-
direction
long step_counter_homingX=1; //initializing homing in X-direction
long step_counter_homingZ=1; //initializing homing in Z-direction
float Step_resolutionX;
boolean rerun=true; //This variable to control the number of time the void loop should run

 // Declaring the stepper motors
```

```
 AccelStepper stepperX(1,2,3); //The 1 stands for easy driver, 2 and 3 are the DIR Pin and STEP Pin of
the driver respectively
 AccelStepper stepperZ(1,4,5);
 Stepper myStepperX(Steps_Per_RevolutionX,2,3);
 Stepper myStepperZ(Steps_Per_RevolutionZ,4,5);

void setup() {

Serial.begin(9600);   // Initialize the Serial monitor with speed of 9600 Bauds// The Homing
procedure
pinMode(Limit_switchX, INPUT_PULLUP);
pinMode(Limit_switchZ, INPUT_PULLUP);
pinMode(EnablePinX, OUTPUT);
pinMode(EnablePinZ,OUTPUT);
pinMode(LED_BUILTIN, OUTPUT);
digitalWrite(EnablePinX,HIGH);
digitalWrite(EnablePinZ,HIGH);
digitalWrite(LED_BUILTIN, HIGH);

  //Set the speed of homing
  myStepperX.setSpeed(500);



Serial.println("The stepper motor is homing in X-direction");

while (digitalRead(Limit_switchX)== LOW) {
    myStepperX.step(step_counter_homingX);
    step_counter_homingX+=1;
  }

  step_counter_homingX=-1;

  while (digitalRead(Limit_switchX)== HIGH) {
    myStepperX.step(Limit_switchX);
    step_counter_homingX-=1;
  }

  stepperX.setCurrentPosition(0);

Serial.println("Stepper X homing is completed");

//Homing the stepper motor in the languimir probe in Z-direction

//Serial.println("The stepper motor is homing in the Z-direction");

myStepperZ.setSpeed(500);
```

```
Serial.println("The stepper motor is homing in Z-direction");

  while (digitalRead(Limit_switchZ)== LOW) {  // Make the Stepper move towards the direction of the
switch until it hits the switch
    myStepperZ.step(step_counter_homingZ);
    step_counter_homingZ+=1;
  }

  myStepperZ.setSpeed(500);
  step_counter_homingZ=-1;

while(digitalRead(Limit_switchZ)== HIGH) {
    myStepperZ.step(step_counter_homingZ);
    step_counter_homingZ-=1;

  }

  stepperZ.setCurrentPosition(0);

Serial.println("Stepper Z homing is completed");

  //Serial.println("Homing Completed !");
  delay(500);


 //Setting the speed of the stepper motor for scanning
  myStepperX.setSpeed(500);
  myStepperZ.setSpeed(500);

digitalWrite(EnablePinX,LOW);
digitalWrite(EnablePinZ,LOW);

  }
void loop() {


float number_of_stepsX;
float number_of_stepsZ;
float Lateral_resolutionX=5; //unit (mm)
float Lateral_resolutionZ=5; //unit (mm)
float Distance_Per_RevolutionX=0.31;
float Distance_Per_RevolutionZ=0.31;
const float  Max_distance_LdriveX=60; //unit (mm)
const float  Max_distance_LdriveZ=60; //unit (mm)
float Time_for_measurementsX=1000; // unit(ms)
float Time_for_measurementsZ=1000; //unit(ms)
float Step_resolutionX;
float Step_resolutionZ;
```

```
float movementX;
float movementZ;
float Max_stepsX;
float Max_stepsZ;

if (rerun == true) {

number_of_stepsX=(Lateral_resolutionX*Steps_Per_RevolutionX)/(Distance_Per_RevolutionX);//Her
e we calculate the number of steps necessary for a given lateral resolution that gives the number of
data points along the distance.
Step_resolutionX=(Lateral_resolutionX*Steps_Per_RevolutionX)/(Distance_Per_RevolutionX);//Here
we initiate the variable that will serve in the equation for moving the linear drive in equal lateral
distances
number_of_stepsZ=(Lateral_resolutionZ*Steps_Per_RevolutionZ)/(Distance_Per_RevolutionZ);//Sam
e as above but for Z
Step_resolutionZ=(Lateral_resolutionZ*Steps_Per_RevolutionZ)/(Distance_Per_RevolutionZ);//Same
as above but for Z.
Max_stepsX=(Max_distance_LdriveX*Steps_Per_RevolutionX)/Distance_Per_RevolutionX;//Used to
calculate the number of steps for the maxiumum distance traveled by the linear drive
Max_stepsZ=(Max_distance_LdriveZ*Steps_Per_RevolutionZ)/Distance_Per_RevolutionZ;//Same as
above but for Z.


Serial.println("The stepper motor is scanning in +Z");
delay(100);
int j=0;
while(number_of_stepsZ < Max_stepsZ && (j<=50))
  {
Serial.println("The stepper motor is scanning in +X");
delay(100);
int i=0;
 while (number_of_stepsX < Max_stepsX && (i<=50)){
   digitalWrite(EnablePinX,HIGH);
   movementX=number_of_stepsX-(i*Step_resolutionX); // The counter i is used to move at equal
rotation steps and thus equal lateral distances
   Serial.println(i);
   Serial.println(movementX);
   Serial.println(number_of_stepsX);
   myStepperX.setSpeed(500);
   myStepperX.step(-movementX);
   digitalWrite(EnablePinX,LOW);
   delay(Time_for_measurementsX);
   number_of_stepsX+=Step_resolutionX;
   i+=1;
  }
Serial.println("The stepper motor is scanning in +Z");
digitalWrite(EnablePinZ,HIGH);
movementZ=number_of_stepsZ-(j*Step_resolutionZ);
```

```
Serial.println(j);
Serial.println(movementZ);
Serial.println(number_of_stepsZ);
myStepperZ.step(movementZ);
digitalWrite(EnablePinZ,LOW);
delay(Time_for_measurementsZ);
number_of_stepsX=(Lateral_resolutionX*Steps_Per_RevolutionX)/(Distance_Per_RevolutionX);
//Here we must renitialize the number_of_stepsX to start a new loop.
number_of_stepsX=-number_of_stepsX; //In order to move in the other direction
Max_stepsX=-Max_stepsX; // The maximum distance in the other direction
Serial.println("The stepper is scanning in -X");
delay(100);
i=0;
 while (number_of_stepsX > Max_stepsX && (i<=50)){ //now the scanning in the other direction has
started so the number of steps is negative so it is higher than Max_step
    digitalWrite(EnablePinX,HIGH);
    movementX=number_of_stepsX+(i*Step_resolutionX);
    Serial.println(i);
    Serial.println(movementX);
    Serial.println(number_of_stepsX);
    myStepperX.setSpeed(500);
    myStepperX.step(-movementX);
    digitalWrite(EnablePinX,LOW);
    delay(Time_for_measurementsX);
    number_of_stepsX-=Step_resolutionX;
    i+=1;
  }
number_of_stepsX=-number_of_stepsX;
number_of_stepsZ+=Step_resolutionZ;
j+=1;
 }
Serial.println("Scan Completed");
digitalWrite(LED_BUILTIN, HIGH);
stepperX.setCurrentPosition(Max_stepsX);
stepperZ.setCurrentPosition(Max_stepsZ);
digitalWrite(EnablePinX,LOW);
digitalWrite(EnablePinZ,LOW);

//stepper.setCurrentPosition(-number_of_steps)
rerun = false;
}

}
```